ELSEVIER

Contents lists available at ScienceDirect

# **International Journal of Mechanical Sciences**

journal homepage: www.elsevier.com/locate/ijmecsci





# Heterogeneous hybrid resolved–unresolved CFD–DEM coupling for fluid–particle interactions

Hao Chen, Shiwei Zhao \*, Jidong Zhao \*

Department of Civil and Environmental Engineering, The Hong Kong University of Science and Technology, Hong Kong Special Administrative Region

#### ARTICLE INFO

Keywords:
Multiphase flow
Fluid-solid interaction
CFD-DEM
Hybrid unresolved-resolved coupling
Arbitrary particle shape
Gap-graded clogging

#### ABSTRACT

This paper presents a novel hybrid resolved–unresolved and heterogeneous-parallel coupling framework for simulating fluid–particle interactions with non-spherical particles of arbitrary geometries. The framework integrates Computational Fluid Dynamics (CFD) and Discrete Element Method (DEM) to dynamically assigns resolved (Immersed Boundary Method) and unresolved (drag force model) coupling schemes based on local particle-to-fluid length scale ratios. This approach optimizes computational efficiency while preserving accuracy, particularly in gap-graded and polydisperse systems. It features the following key innovations: (1) An advanced DEM solver enhanced by ray-tracing techniques, facilitating high-performance contact detection for arbitrary particle morphologies (e.g., CT-scanned grains); (2) A robust volumetric-weighted hybrid coupling method that ensures smooth and stable momentum exchange between fluid and particles; (3) A CPU–GPU heterogeneous coupling interface that supports asynchronous computation and data transfer, incorporating novel signed-distance fields and marker-based particle-shape-fluid mapping. The framework has been validated against analytical solutions and various experimental benchmarks, demonstrating its accuracy, robustness, and efficiency. It serves as a scalable and shape-aware tool for modeling multiphase systems across diverse fields, including large-scale and complex geomechanics, chemical engineering, and industrial processes.

## 1. Introduction

Complicated interactions between granular materials and fluids are prevalent in both natural phenomena and industrial processes. To investigate the mechanisms that govern particle-fluid mixtures, researchers have developed coupled frameworks that are applicable across various contexts, including deep-sea mining [1–3], seepage phenomena [4–6], clogging issues [7–9], erosion challenges [10–14], and fluidized beds [15–17]. A prominent approach within these hybrid frameworks is Eulerian–Lagrangian coupling [18,19]. In this methodology, the Eulerian component utilizes CFD to continuously capture the dynamic behavior of fluids, while the Lagrangian aspect, represented by DEM, is employed to simulate granular materials [20–24].

There are two prevailing CFD–DEM coupling schemes: particle-resolved and particle-unresolved schemes [25]. The resolved scheme accounts for particle–fluid interactions at the discretized sub-surface of each particle [26], requiring an Eulerian mesh that is comparable to or smaller than the size of the particles. In contrast, the unresolved scheme treats these interactions empirically, focusing on the scale of the CFD decomposition (or mesh) [27]; thus, the fluid mesh is significantly larger than the particles, typically at least three times the particle diameter. Given the variance in length scale ratios between particles

The shape of particles is fundamental to both coupling schemes [36]. Unlike spherical particles, non-spherical particles exhibit anisotropic rotation. Specifically, the alignment of their major and minor axes with the streamwise direction of the fluid produces markedly different interaction responses [37]. This anisotropic behavior has significant implications for the properties of multiphase mixtures, affecting aspects such as fabric anisotropy [38], packing porosity [39,40], and stress distributions [41]. Consequently, failing to adequately account for particle shape can lead to inaccurate or misleading results [42–46].

Substantial efforts have been dedicated to understanding the influence of particle shape on the coupling of CFD and DEM. Early models simplified non-spherical particles by approximating them as either spheres or clusters of spheres [47–49]. In the context of resolved coupling, where larger particle-to-fluid ratios highlight the significance of shape effects, more advanced shape representations have emerged. These include super-ellipsoids, which allow for the independent adjustment of elongation and angularity [50], as well as

E-mail addresses: ceswzhao@ust.hk (S. Zhao), jzhao@ust.hk (J. Zhao).

and fluid cells, the dynamic corrections applied differ accordingly. For instance, the Immersed Boundary Method (IBM) [28–30] is utilized in the resolved regime [31–34]. Conversely, in the unresolved regime, a drag force model is commonly employed [35].

<sup>\*</sup> Corresponding authors.

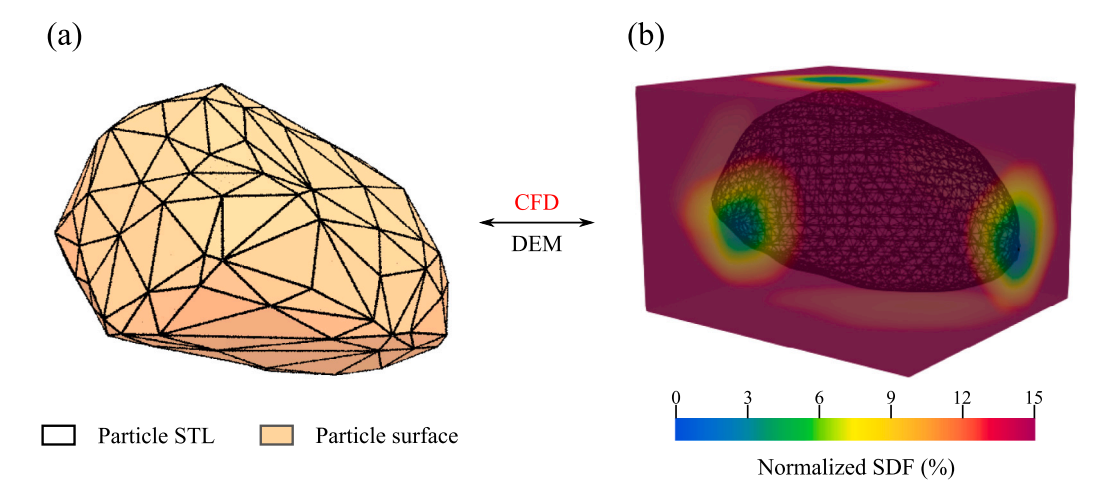
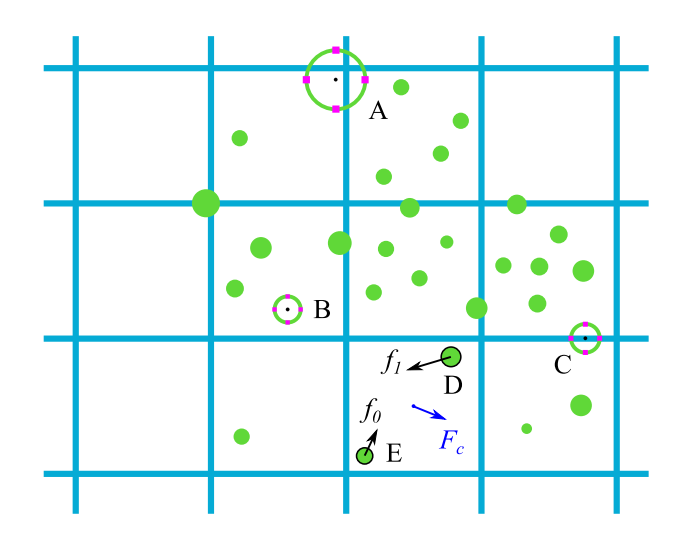


Fig. 1. Determination of the SDF template for arbitrarily shaped particles, encoded from (a) the DEM shape to (b) the CFD solution domain. Note: The color gradient from blue to red represents increasing SDF values outward from the particle surface.



**Fig. 2.** Imposition of drag force between fluid and particles in the unresolved coupling scheme. Note that particle influence is interpolated to the fluid based on the volumetric fraction distribution, weighted by the magenta markers in neighboring cells.

Partial immersed  $V_c$ Cell B  $V_c$   $V_c$ Cell B

Fig. 6

Particle O  $V_p$   $V_p$   $V_c$ Cell A

Fully immersed

**Fig. 3.** Imposition of immersed boundary force between fluid and particles in the resolved coupling scheme, and the force is weighted by the particle's occupied volume within each cell.

arbitrary shape methodologies like the Mesh-based Overlapping Arbitrary Lagrangian–Eulerian (MOALE) approach [25,51], Signed-Distance Fields (SDF) [52], the Large-Interface Model (LIM) [53], and Image-based PARticles (IPAR) [54]. In the unresolved coupling regime, where particles are smaller than the fluid-cell scale, research has focused on enhancing drag force models. This includes the development of non-spherical drag force correlations [55] and higher-order drag force interpolation techniques, such as semi-resolved methods [56–58].

Despite recent advancements, the application of CFD–DEM in engineering contexts continues to present significant challenges. A primary concern is the substantial computational overhead associated with accurately capturing variations in particle-size distributions (PSDs) and shapes. Fully resolved approaches impose stringent mesh-size requirements due to the presence of numerous fine and highly distorted grains. While adaptive mesh refinement techniques, as discussed in [59], can alleviate some of these computational challenges, they introduce new considerations regarding regridding frequency, refinement levels, and selection of refinement methods. Conversely, fully unresolved

approaches enhance computational efficiency but may compromise fidelity, particularly in scenarios where near-particle-field hydrodynamics and particle shape effects are critical. Moreover, when addressing various classes of particle shapes, the calibration of drag laws for each case becomes impractical, thereby limiting the generalizability of the approach.

To tackle these challenges, we propose a hybrid resolved–unresolved strategy. This framework adaptively categorizes each particle into either the resolved or unresolved coupling based on its particle-to-fluid length-scale ratio. The resolved branch utilizes an arbitrary-shape DEM model to accurately capture the effects of particle shape with greater fidelity. In contrast, the unresolved branch employs drag-force models augmented with higher-order interpolation techniques, enhancing the balance between accuracy and computational efficiency. Both branches operate within a collaborative CPU–GPU architecture: the CFD solver is executed on CPUs, while DEM tasks, such as arbitrary-shape contact detection, shape encoding from DEM to CFD, and the

transfer of state updates from CFD back to DEM, are processed on massively parallel GPUs. This design not only distributes memory across devices but also significantly improves scalability, making it suitable for engineering-scale applications of hybrid CFD-DEM systems.

The structure of this paper is organized as follows: Section 2 provides an overview of both unresolved and resolved CFD–DEM coupling approaches, accompanied by a description of our arbitrary-shape DEM model. In Section 3, we detail the methodology underpinning the proposed hybrid unresolved–resolved CFD–DEM coupling framework. Section 4 presents benchmark results for the three coupling solvers. Subsequently, Section 5 includes two numerical examples of fluid-driven clogging, demonstrating how the hybrid framework effectively harnesses the strengths of both resolved and unresolved methods within a gap-graded multiphase system. Finally, Section 6 concludes with a summary of the key findings.

#### 2. General CFD-DEM coupling

This section outlines the governing equations and specific implementations of the CFD and DEM solvers, highlighting the characteristics of both unresolved and resolved coupling strategies used in this study. It provides detailed information on the encoding of particle shapes from the DEM model to the CFD framework, the computation of hydrodynamic forces from CFD to DEM, and the corresponding numerical iteration strategies employed.

#### 2.1. Ray-Tracing DEM

Our previously proposed framework, Ray-Tracing DEM (RTDEM) [60], accommodates a diverse array of particle shape models, spanning from mathematically defined geometries such as spheres, ellipsoids, and super-ellipsoids to arbitrary forms exemplified by the sand grain illustrated in Fig. 1(a). The sand grain geometry utilized throughout this study exhibits a sphericity of 0.914, an aspect ratio of 1.37, and a mean surface curvature of 0.024. Since subsequent benchmarks and examples involving arbitrary shapes consistently reference this geometry, we refrain from repeating these descriptors in the ensuing sections.

Central to the RTDEM framework is a Ray-Tracing-Based contact algorithm specifically designed for arbitrary shapes. This method harnesses the processing power of NVIDIA GPUs equipped with RT cores and systematically organizes each particle's geometry into a structured hierarchy comprising volumes, faces, edges, and vertices. Ray queries navigate this hierarchy to swiftly identify potential contact pairs through intersection tests with geometric primitives. The combination of hardware-accelerated traversal and intersection, along with various software optimizations, results in significant efficiency improvements compared to traditional CPU-based DEM implementations (e.g., IPAR representations).

Figs. 1(a) and (b) illustrate the formation of a hierarchical structure for a sand grain in RTDEM and its corresponding SDF, respectively. This SDF facilitates the representation of arbitrary particle shapes, bridging the gap between DEM and CFD, as discussed in [61]. Each distinct shape possesses a unique SDF template, which is initialized only once at the first time step and remains constant throughout the simulation. When a particle undergoes rotation or scaling, an affine transformation is applied to the initial SDF template, enabling rapid querying of the updated SDF without the need to recalculate the entire SDF.

# 2.2. Unresolved CFD-DEM coupling

The unresolved coupling between CFD and DEM requires a dynamics adjustment governed by a drag force law. This law quantifies the resistance encountered by particles as they traverse a fluid. In conjunction with additional forces, such as pressure gradient, viscous force,

and buoyancy, these elements culminate in the governing equations of  $\overline{\text{DEM}}$ :

$$m_i \frac{dU_i^p}{dt} = \sum_{i=1}^{n_i^c} F_{ij}^c + F_i^f + F_i^g,$$
 (1a)

$$I_i \frac{d\boldsymbol{\omega}_i^p}{dt} = \sum_{i=1}^{n_i^c} \boldsymbol{M}_{ij}^c, \tag{1b}$$

$$F_{i}^{f} = F_{i}^{p} + F_{i}^{v} + F_{i}^{d} + F_{i}^{buo}. {1c}$$

where  $U_i^p$  and  $\omega_i^p$  denote the translational and rotational velocities of particle i, respectively. The terms  $F_{ij}^c$  and  $M_{ij}^c$  represent the contact force and torque arising from the interaction between DEM contact pairs of particles i and j. The net force exerted by the fluid on solid particle i is captured by  $F_i^f$ , which may encompass the pressure gradient  $F_i^p$ , viscous force  $F_i^v$ , drag force  $F_i^d$ , and buoyancy  $F_i^{buo}$ . Moreover,  $F_i^g$  indicates the gravitational force acting on particle i. The variables  $m_i$  and  $I_i$  signify the mass and moment of inertia of particle i, respectively.

We assume isothermal and incompressible flow in our CFD analysis, utilizing a volume-averaged approach to facilitate coupling with the DEM. Consequently, the continuity equation for the fluid–particle two-phase system is expressed as follows:

$$\frac{\partial(\epsilon\rho)}{\partial t} + \nabla \cdot (\epsilon\rho U^f) = 0. \tag{2}$$

where  $U^f$  represents the average intrinsic velocity of the fluid within the cell,  $\epsilon$  denotes the volume fraction of the fluid in the cell, and  $\rho$  is the fluid density.

The momentum conservation equation for the incompressible twophase equation reads:

$$\frac{\partial (\epsilon \rho \mathbf{U}^f)}{\partial t} + \nabla \cdot (\epsilon \rho \mathbf{U}^f \mathbf{U}^f) = -\epsilon \nabla p + \nabla \cdot (\epsilon \mu \nabla \mathbf{U}^f) - \mathbf{F}^d + \epsilon \rho \mathbf{g}. \tag{3}$$

where p represents the pressure within the fluid cell,  $\mu$  denotes the dynamic viscosity of fluid,  $F^d$  indicates the drag force resulting from fluid–particle interactions, and g represents the gravitational acceleration.

The imposition of drag force is illustrated in Fig. 2. For further details, please refer to Appendix A.

## 2.3. Resolved CFD-DEM coupling

The dynamic correction within the resolved CFD–DEM coupling is achieved through the Immersed-Boundary force (IB force), denoted as  $F_{IB}$ , which is implemented using the Immersed Boundary Method (IBM). The governing equation for the CFD component is expressed as follows:

$$\frac{\partial \rho}{\partial t} + \nabla \cdot (\rho U^f) = 0, \tag{4a}$$

$$\frac{\partial(\rho U^f)}{\partial t} + \nabla \cdot (\rho U^f U^f) = -\nabla p + \nabla \cdot (\mu \nabla U^f) + \rho g + F_{IB}. \tag{4b}$$

The governing equations for the DEM are formulated as follows:

$$m_i \frac{dU_i^p}{dt} = \sum_{j=1}^{n_i^c} F_{ij}^c + \sum_{j=1}^{n_i^{cell}} F_{ij}^{IB} + F_i^g + F_i^{buo},$$
 (5a)

$$I_{i}\frac{d\omega_{i}^{p}}{dt} = \sum_{i=1}^{n_{i}^{c}} M_{ij}^{c} + \sum_{i=1}^{n_{i}^{cell}} T_{ij}^{IB},$$
 (5b)

$$T_{ij}^{IB} = (\vec{r_c} - \vec{r_p}) \times F_{ij}^{IB}. \tag{5c}$$

where  $F_{ij}^{IB}$  and  $T_{ij}^{IB}$  denote the force and torque exerted on particle i by the jth cell's IB force through the IBM. The vectors  $\vec{r_c}$  and  $\vec{r_p}$  represent the position of cell j and particle i, respectively. And  $F_i^{buo}$  signifies the buoyant force acting on particle i.

Fig. 3 illustrates the generation of the force  $F^{IB}$  and the torque  $T^{IB}$ . The shape domain of Particle O is represented by the green region,

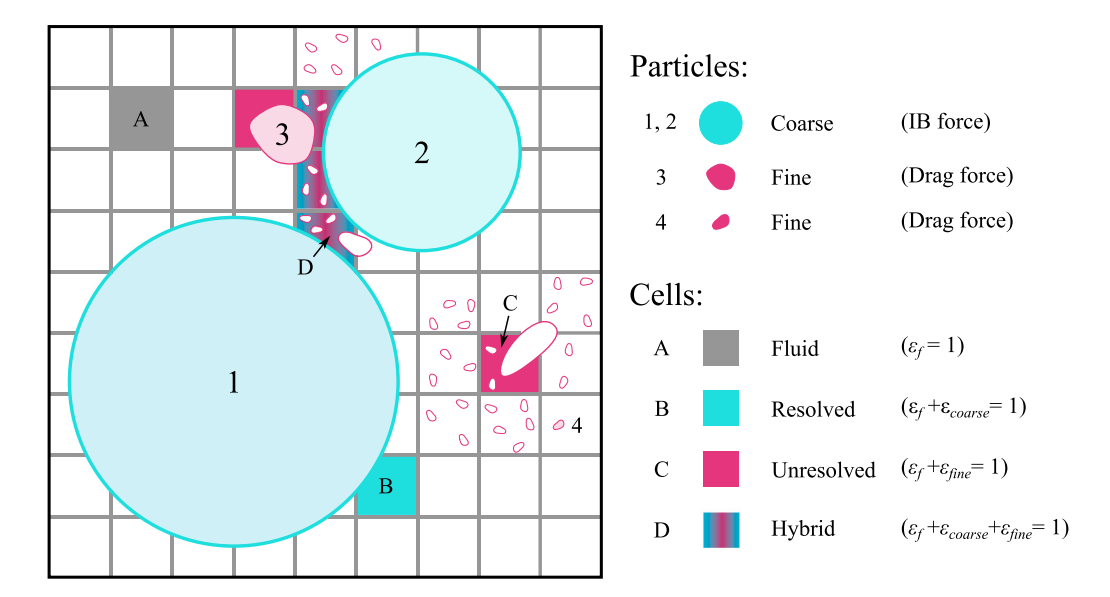


Fig. 4. A hybrid approach integrating both resolved and unresolved components: coarse particles (1, 2) are mapped to fluid cells B and D, while fine particles (3, 4) are mapped to cells C and D. Note that particle sizes are normalized relative to the neighboring cell size.

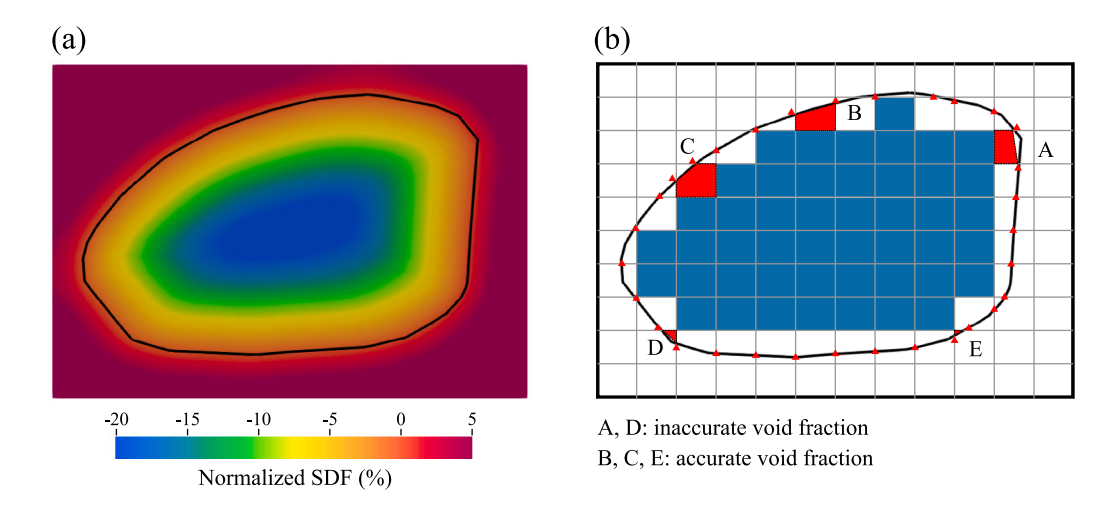


Fig. 5. Calculation of void fraction for arbitrarily shaped particles in resolved coupling, and the classification of a cell as inside or outside the particle is determined by (a) the averaged SDF values from its (b) vertices.

which may not conform to the geometry of the surrounding structured cells. As a result, the relative positions of the cells with respect to the particle can be categorized as fully immersed cells (Cell A) and partially immersed cells (Cell B). Considering the translational velocity of Particle O as  $\boldsymbol{v}_p$  and its rotational velocity as  $\boldsymbol{\omega}_p$ , the effective velocity projection from the particle to the cells, denoted as  $\boldsymbol{v}_c'$ , is defined by the equation:  $\boldsymbol{v}_c' = \boldsymbol{v}_p + (\overline{\boldsymbol{r}_c} - \overline{\boldsymbol{r}_O}) \times \boldsymbol{\omega}_p$ . For partially immersed cells, the projected velocity requires an additional correction based on the fluid volume fraction  $\boldsymbol{\varepsilon}_f$ , and is expressed as:  $\boldsymbol{v}_c' = (1 - \boldsymbol{\varepsilon}_f) \boldsymbol{U}_c^f + \boldsymbol{\varepsilon}_f \boldsymbol{v}_c'$ , where  $\boldsymbol{U}_c^f$  denotes the fluid velocity within the cell.

The IB force is described by Eq. (6). For additional details, please consult Appendix B.

$$F_{IB} = \frac{v_c' - U_c}{A}.\tag{6}$$

where A represents the coefficient matrix from Eq. (4).

## 3. Hybrid resolved-unresolved CFD-DEM coupling

This section delineates the governing equations and implementation details of the hybrid CFD–DEM coupling framework proposed in this study. It elaborates on the mapping strategy between particles and fluid cells, describes the adaptive predictor–corrector iteration workflow, and discusses the parallel techniques implemented within a CPU–GPU topology.

# 3.1. Hybrid coupling scheme

The ratio of particle size to fluid cell size is a pivotal determinant in selecting between unresolved and resolved coupling schemes in conventional research. Prior investigations suggest that resolved coupling schemes are advantageous when the particle-to-cell ratio exceeds approximately 5. Conversely, unresolved schemes are more applicable when this ratio falls below roughly 0.3 to 0.4. For intermediate scenarios, a semi-unresolved approach is typically recommended [63].

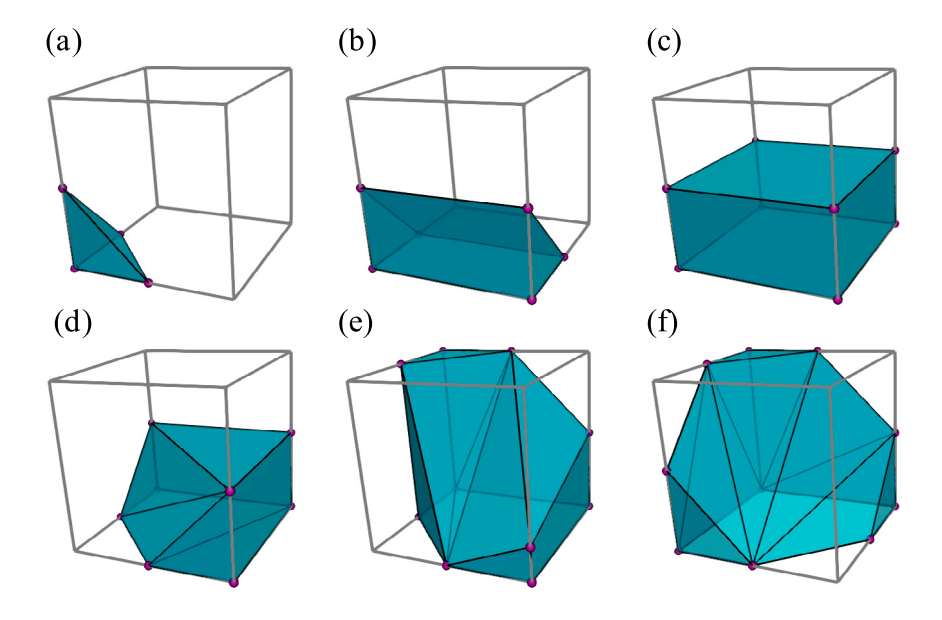


Fig. 6. Types of intersection volumes between an arbitrarily shaped particle and a CFD cell, classified using the marching cubes algorithm.

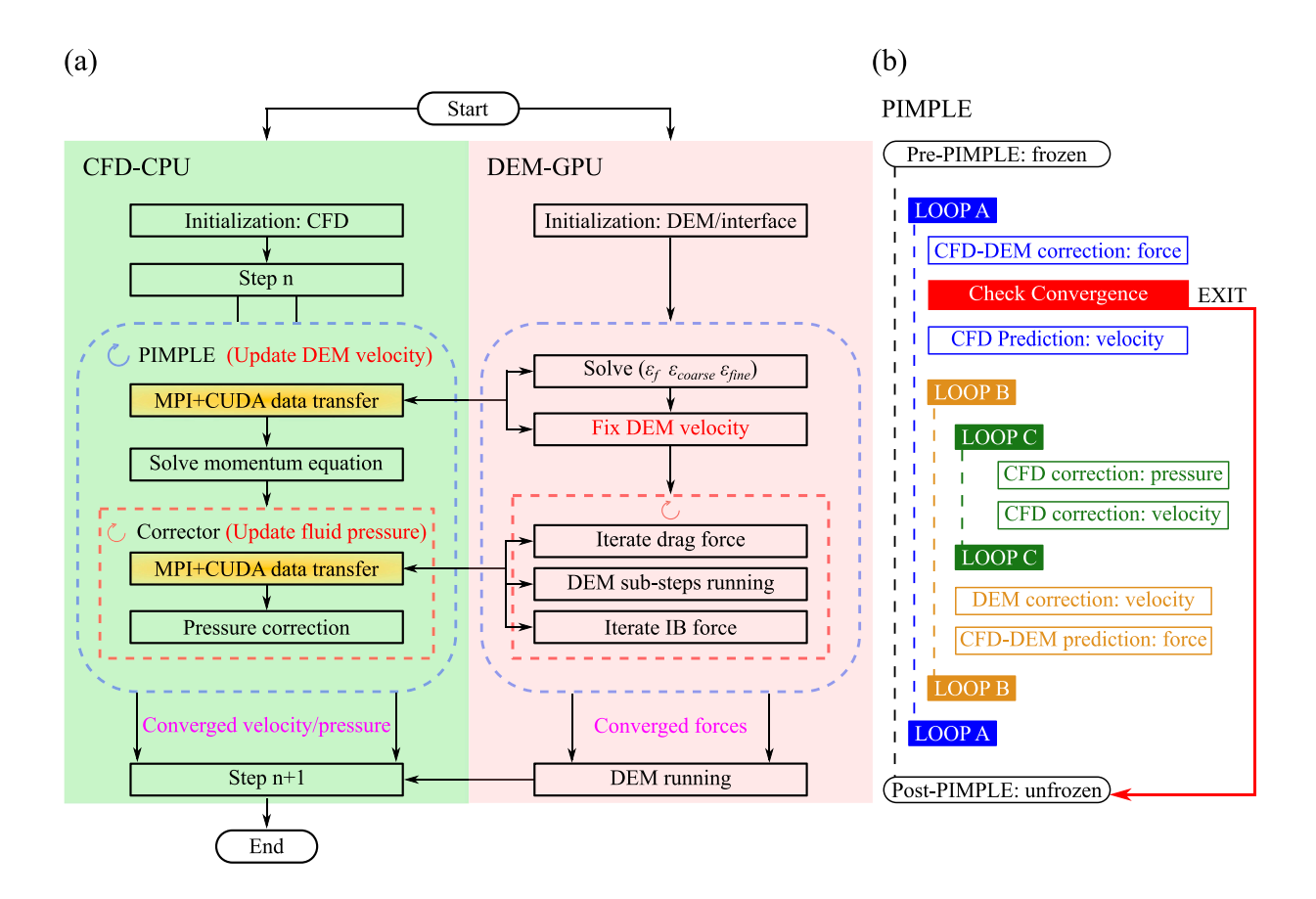


Fig. 7. Flowchart of the proposed hybrid framework: (a) CFD executed on the CPU (green box) and DEM executed on the GPU (red box), connected via (b) the CFD-DEM PIMPLE workflow.

However, when dealing with gap-graded features or continuous distributions with significantly wide size ranges, either purely unresolved or resolved schemes can become impractical, as the balance between computational accuracy and overhead is compromised. Our proposed

hybrid coupling method effectively addresses this challenge by adaptively assigning the appropriate coupling mode for each particle based on its local size in relation to neighboring cells. This adaptive approach renders it suitable for various particle size distribution configurations,

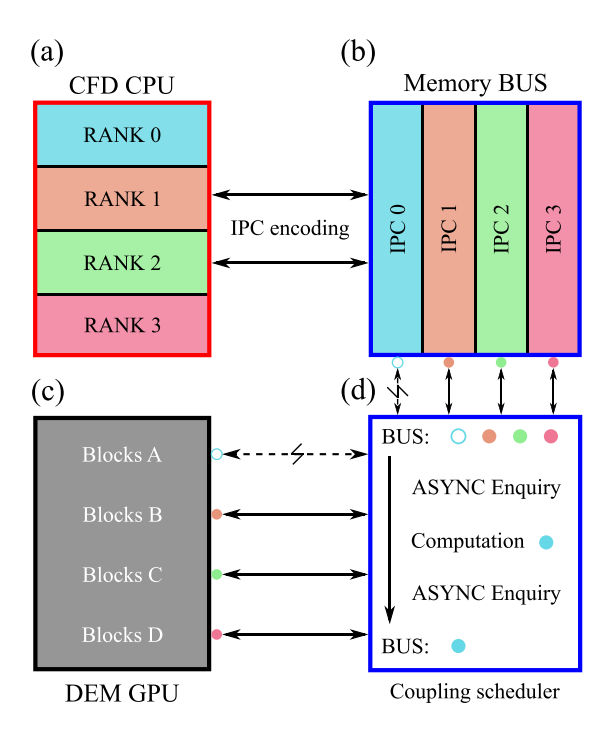


Fig. 8. Topology of data transfer between CFD and DEM: (a) CPU MPI configuration, (b) CPU mapping to GPU, (c) GPU memory layout, and (d) memory and computational scheduler.

whether monodisperse or gap-graded.

A representative scenario illustrating the selection of a particle-wise coupling scheme is shown in Fig. 4. Three distinct particle-to-cell size ratios are presented: coarse particles (1 and 2) with a size ratio of 6:1, medium-sized particles (3) with a 1:1 ratio, and fine particles (4) with a 0.35:1 ratio. Our hybrid solver detects these characteristics and assigns a pure resolved scheme for coarse particles, a pure unresolved scheme for fine particles, and a resolved–unresolved blending mode for medium-sized particles. As a result, neighboring fluid cells are classified into four categories: pure resolved cells (B), pure unresolved cells (C), hybrid cells (D), and pure fluid cells (A). Each type of fluid cell is associated with a specific volumetric index to facilitate particle–fluid dynamics correction:  $\epsilon_{coarse}$  for coarse particles,  $\epsilon_{fine}$  for fine particles, and  $\epsilon_f$  for pure fluid.

It is essential to recognize that specific assumptions govern the behavior of blending mode cells (D):

- The blending cell domain is engineered to achieve a uniform integration of the mechanical properties of coarse particles, fine particles, and fluids, despite the potential for a non-uniform distribution of their actual positions.
- The blending cell initially corrects the fluid dynamics by employing the immersed boundary method for coarse particles, as described by the following equation:

$$U_{conv} = (U_p \epsilon_{coarse} + U_f \epsilon_f). \tag{7}$$

where  ${\it U}_p$  represents the coarse particle velocity projected onto the local cell, and  ${\it U}_f$  denotes the local fluid velocity.

 The dynamics correction of the blending cell is subsequently refined through a staggered update procedure that integrates the immersed boundary solver with the drag force model, ultimately iterating towards an equilibrium state. Based on the assumptions outlined above, the momentum equations for the resolved–unresolved-blending cells can be expressed as follows:

$$\begin{split} \frac{\partial [(1-\epsilon_{fine})\rho \boldsymbol{U}_f]}{\partial t} + \nabla \cdot [(1-\epsilon_{fine})\rho \boldsymbol{U}_f \boldsymbol{U}_f] - \nabla \cdot [(1-\epsilon_{fine})\mu \nabla \boldsymbol{U}_f] \\ = -(1-\epsilon_{fine})\nabla p + \boldsymbol{F}^d + \boldsymbol{F}^{IB}. \end{split} \tag{8}$$

where the primary unknowns include the superficial fluid velocity,  $\boldsymbol{U}_f$ , which can take on intermediate values of  $\boldsymbol{U}_f^*$  and  $\boldsymbol{U}_f^{**}$ , in addition to the fluid pressure, p. These primary unknowns will be adjusted by both the drag force, denoted as  $\boldsymbol{F}^d$ , and the IB force, represented as  $\boldsymbol{F}^{IB}$ .

The initial velocity intermediate, denoted as  $U_f^*$ , is derived from the momentum equation, and subsequently contributes iteratively to the correction of the drag force. In hybrid coupling, the drag force not only depends on the velocities of the fine particles and the fluid but is also considerably influenced by the velocity of the coarse particles, weighted by the factor  $\epsilon_{coarse}/(\epsilon_f + \epsilon_{coarse})$ . Thus, the generalized formulation of the drag force model, denoted by the function F, can be expressed as follows:

$$F^{d} = F\{\frac{\epsilon_{coarse}}{\epsilon_{f} + \epsilon_{coarse}}, U^{IB}, U_{f}^{*}, \sum_{i}^{N_{p}} U_{i}^{p2} \omega_{i,pc2}\}.$$
(9)

When the drag force is updated, its value will be utilized to inform the second intermediate fluid velocity ( $U_f^{**}$ ) update in the subsequent solution of the Poisson equation. To ensure an accurate distribution of the drag force among the fine particles, we introduce weights  $\omega_{i,pc2}$ , which represent the volume occupation ratio of each cell within an individual fine particle.

Subsequently, the IB force  $(F^{IB})$  is calculated as the difference between the intermediate second fluid velocity  $(U_f^{**})$  and the IB velocity  $(U^{IB})$ , employing coarse particle weights against the cells denoted as  $\omega_{i,nc}$ :

$$F^{IB} = \rho V_c \frac{(U^{IB} - U_f^{**})}{\Delta t},$$
 (10a)

$$U^{IB} = \frac{\epsilon_f U_f^{**} + \sum_i^{N_p} \omega_{i,pc1} U_i^{p1}}{\epsilon_f + \sum_i^{N_p} \omega_{i,pc1}}.$$
 (10b)

Several physical properties, such as void fraction, velocity, and particle diameter, are essential for calculating both drag forces and IB forces. To interpolate these properties between the particle and cell sides, the weights  $\omega_{i,pc1}$  and  $\omega_{i,pc2}$  are also required, which are determined using either SDF sampling or marker sampling. A smooth interpolation from these weights to their corresponding physical properties is implemented in a manner similar to the semi-unresolved approach proposed by [56], as shown below:

$$\epsilon_{coarse} = \sum_{i}^{N} \omega_{i,pc1},$$
(11a)

$$\epsilon_{fine} = \sum_{i}^{N} \omega_{i,pc2}.$$
 (11b)

# 3.2. Cell-particle mapping: Discretization of the marching cubes SDF

Unresolved coupling utilizes a straightforward marker-based discretization of particles to determine the in/out state concerning the cells. However, when resolved coupling necessitates higher precision, especially in the presence of arbitrarily shaped particles, a SDF is employed to ascertain the in/out state relative to the particle. As illustrated in Fig. 5(b), if all four vertices of a cell possess negative SDF values, the entire cell is deemed to be within the particle domain. Conversely, if none of the vertices have negative SDF values, the cell is classified as completely outside the particle. In all other scenarios, the cell is categorized as partially intersecting with the particle.

Further insights, such as void fraction, can be derived from the discretization process depicted in the cells labeled A through E in Fig.

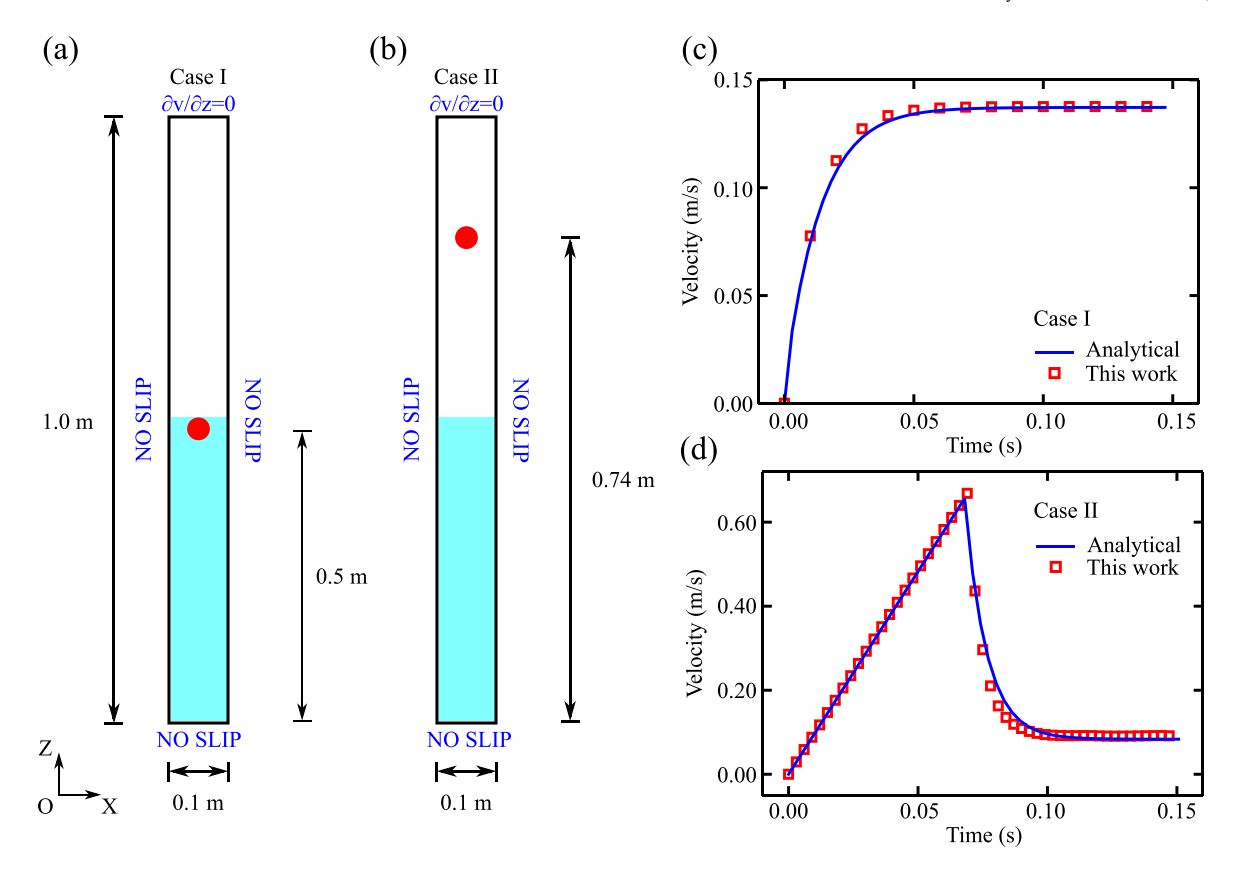


Fig. 9. Entry of a single particle into water: (a, b) illustrations of the experimental setup for simulations of Case I and Case II, and (c, d) the variation of settling velocity over time for both cases.

5(b). Specifically, cells A, B, and C exhibit trapezoidal intersections with the particle, cell D demonstrates a triangular intersection, while cell E shows only a minimal overlap. For each intersection type, the volume is analytically approximated by interpolating SDF values along the edges and vertices of the cells, employing a methodology akin to the marching cubes algorithm [64], as exemplified by the six states in Fig. 6. By systematically iterating over the SDF values at the edges and vertices, we can accurately determine the intersection volume, thereby calculating the void fraction between cells and particles (refer to Algorithm 1).

## Algorithm 1: Register particle within cells of resolved condition.

**Input:** particle number  $N_p$ , particle position p, cell space  $d_{xyz}$ , particle volume  $vol_p$ , cell volume  $vol_c$ , cell number in each dimension  $N_{xyz}$ , particle axis aligned bounding box box, if under resolved coupling  $is_{unresolved}$ 

**Output:** particle index of cells  $p_{id}$ , particle weights of cells  $p_{\omega}$ , void fraction of fluid on cell  $\epsilon_f$ 

```
Volume Traction of Hund on Cen \epsilon_f

1 \epsilon_f = 1;

2 for i \leftarrow 0 to N_p do

3 | xyz = (p[i] \pm 0.5box[i])/d_{xyz};

4 | cell_{id} = [x_{min} : x_{max}] + [y_{min} : y_{max}] * N_x + [z_{min} : z_{max}] * N_x * N_y;

5 | p_{id}[i].append(cell_{id});

6 seq_{id} = [0 : N_p);

7 sort_k ey_value(p_{id}, seq_{id});

8 unique_{cell} = rm_duplicate_element(p_{id});

9 for i \leftarrow 0 to unique_{cell}. size do

10 | vol = SDF(p_{id}[i]);

11 | \epsilon_f[p_{id}[i]] - vol/vol_c[p_{id}[i]];
```

# 3.3. Cell-particle mapping: A many-to-one interpolation parallel technique

We present a novel many-cells-to-one-particle mapping strategy that effectively and consistently accelerates both resolved and unresolved schemes. In this methodology, particles function as executors to establish particle-cell mappings in parallel, tailored to their respective shapes and sizes. A significant challenge arises when multiple particles attempt to modify the same cell simultaneously, potentially leading to race conditions, as illustrated in Algorithm 2. To address this challenge, we implement a hierarchical broad-narrow particle-cell search strategy. During the broad phase, we construct an axis-aligned bounding box (AABB) for each particle, enabling the efficient identification of potentially interacting cells. Only the candidate cells identified in this phase are then passed on to the narrow phase, where detailed exchanges of physical properties take place.

In both unresolved and resolved schemes, particles can be treated as either point-like or shape-aware entities. Their connections to cells are often multiplicative, as illustrated by particle A in Fig. 2 and particle O in Fig. 3. By employing the semi-resolved principles outlined by [56, 65], it becomes evident that the physical properties of particles A and O can be interpolated with greater accuracy through a volumetric-weighted approach that connects them to their respective linking cells. This underscores the necessity of employing a many-cell-to-one-particle method in this section.

# 3.4. Flowchart of the PIMPLE iteration in the hybrid solver

Fig. 7(a) illustrates the individual components of the CFD (represented by the green box) and DEM (denoted by the red box) solvers. Meanwhile, Fig. 7(b) presents an overview of the organization of these components within the hybrid CFD-DEM PIMPLE workflow. Notable

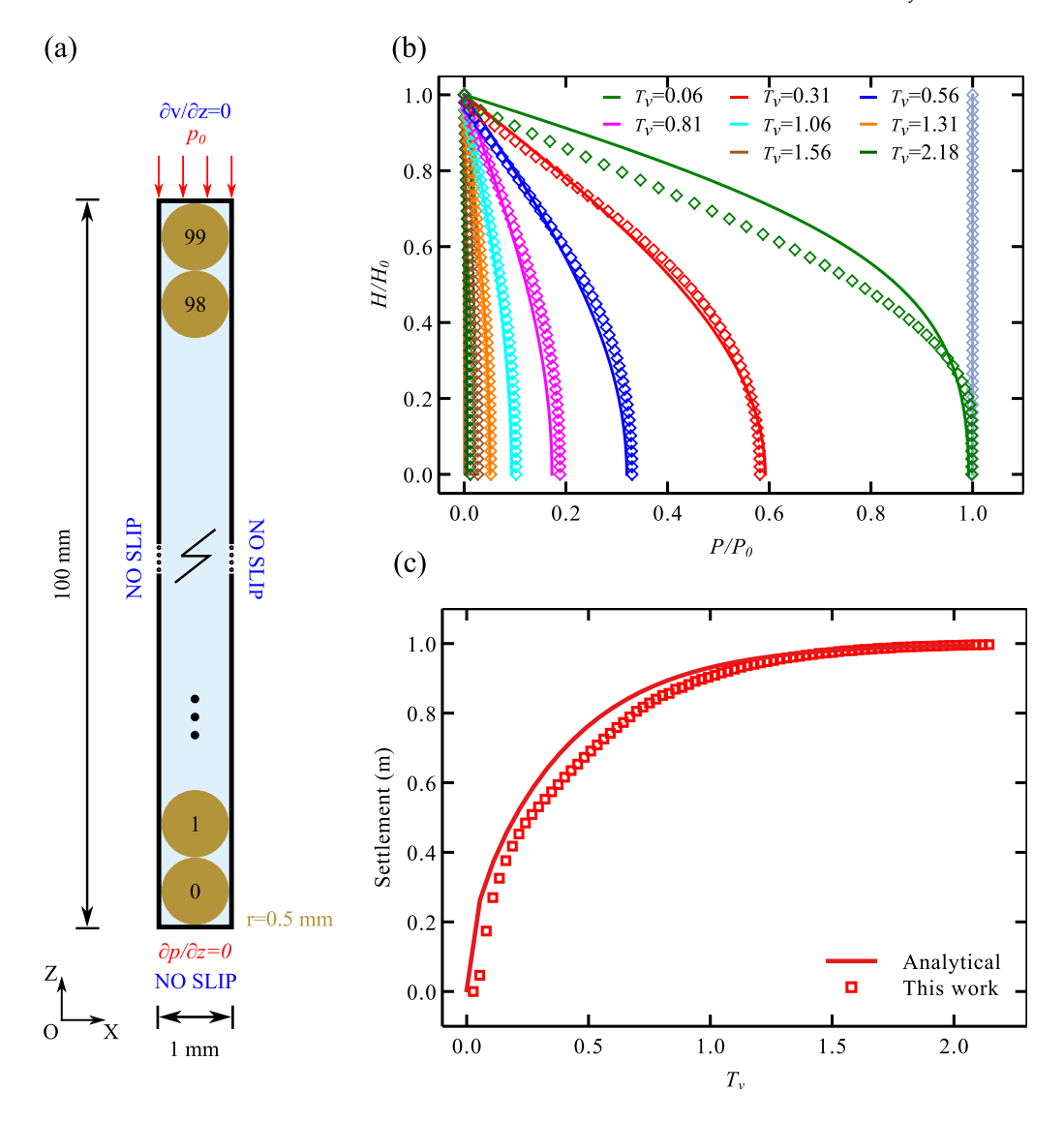


**Fig. 10.** One-dimensional consolidation characterized by: (a) the initial simulation configuration, (b) the progression of pressure distribution along the vertical axis, and (c) the settlement of the uppermost particle as a function of the dimensionless time factor  $T_a$ .

differences from the traditional CFD PIMPLE methodology include the computation of the void fraction, determination of interpolation weights, adjustment of DEM dynamics, and data transfer processes, all highlighted in the yellow box.

At each timestep, the CFD–DEM PIMPLE algorithm initiates with the Pre-PIMPLE stage, during which the void fraction and interpolation weights linking the CFD and DEM are established. These interpolation weights are calculated using particle-marker decomposition for the unresolved scheme, an SDF-based marching-cube technique for the resolved scheme, or a combination of both in the case of hybrid coupling. Once determined, the weights, along with DEM velocities, are frozen and subsequently transmitted to the LOOP stage of the CFD–DEM PIMPLE.

The LOOP stage comprises three nested loops, designated A, B, and C, in order from outermost to innermost (see Fig. 7(b)). In Loop A, the algorithm updates the CFD–DEM interaction forces and predicts the fluid velocity, which then leads into Loop B. Within Loop B, the predicted fluid velocity undergoes iterative corrections to meet the continuity criterion, while pressure adjustments take place in Loop C. The updated fluid properties are subsequently utilized to recompute the

interaction forces, which are then applied to modify the velocities of the DEM particles. At the conclusion of Loop B, a convergence check is performed; if the criterion is met, the algorithm proceeds to the Post-PIMPLE stage, where the DEM variables are unfrozen and corrected using the converged interaction forces, which are then advanced through the DEM solver via Newton integration. If the criterion is not satisfied, the algorithm returns to Loop A for further iterations.

This LOOP stage synthesizes both IB and drag forces into a cohesive representation of interaction forces, facilitating the integration of different force models or coupling strategies without necessitating changes to the overall CFD-DEM PIMPLE structure. Furthermore, one might ponder why the CFD-DEM PIMPLE updates the CFD mechanical properties directly, while DEM variables are subjected to a frozen-unfrozen approach. This distinction arises from the observation that DEM dynamics typically progress over a more microscopic timescale than CFD. By freezing DEM variables during the inner PIMPLE iterations, we mitigate small velocity fluctuations that could compromise the stability of the implicit CFD solver, which demands a stricter convergence criterion compared to that of DEM.

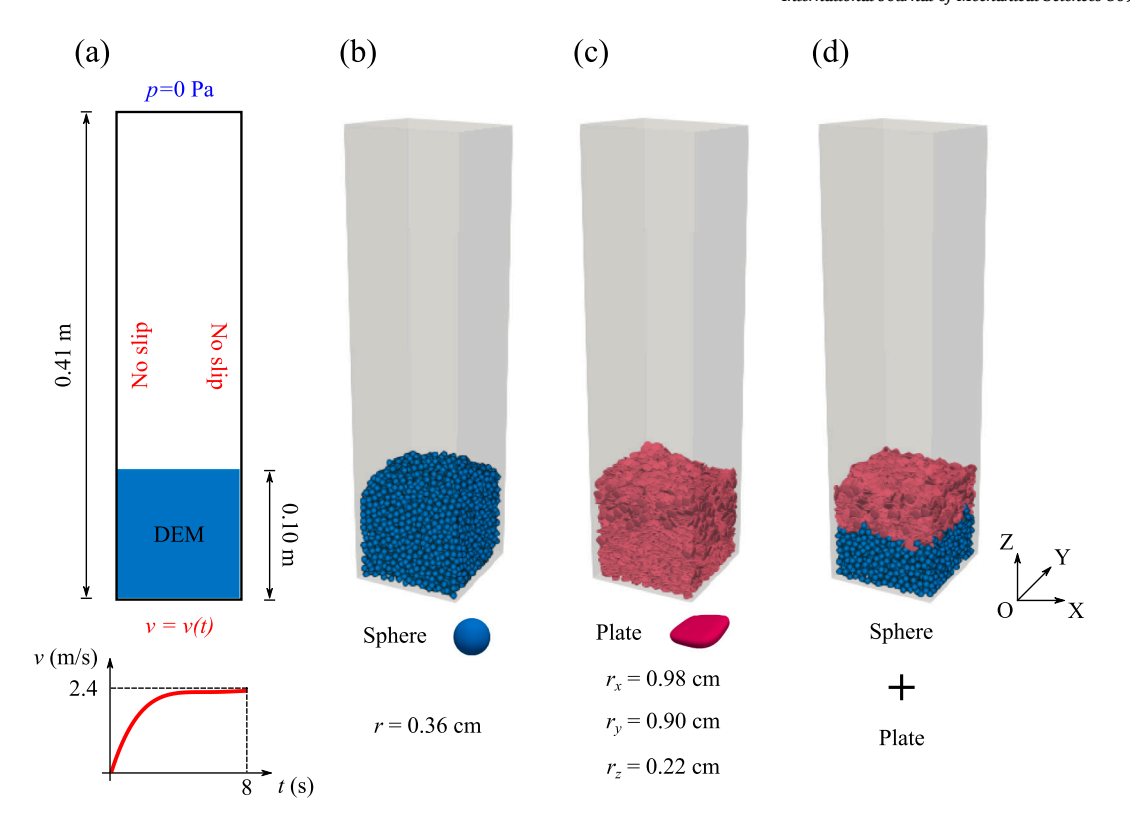


Fig. 11. Ergun test: (a) simulation configurations, (b) spheres packing, (c) plates packing, and (d) mixture of spheres and plates.

Algorithm 2: Register particles within cells exhibiting unresolved conditions.

**Input:** particle number  $N_p$ , particle position p, cell space  $d_{xyz}$ , particle volume  $vol_p$ , cell volume  $vol_c$ , cell number in each dimension  $N_{xyz}$ , particle axis aligned bounding box **Output:** particle index of cells  $p_{id}$ , void fraction of fluid on cell

# 3.5. CPU-GPU heterogeneous acceleration framework

The open-source CFD-DEM framework CFDEM® [66], which integrates the OpenFOAM CFD solver [67] with the LIGGGHTS DEM solver [68], has gained significant prominence in the fluid-particle interaction community. Despite the growing adoption of GPU technologies, exemplified by GPU-based CFD frameworks such as FUN3D-GPU [69] and GPU-accelerated DEM implementations like GeoTaichi-DEM [70], CPU-parallel frameworks remain the dominant approach for CFD-DEM coupling. This preference stems from fundamental architectural trade-offs between CPUs and GPUs [71]: CPUs typically provide larger memory capacity but fewer parallel cores, whereas GPUs offer massive parallelism with comparatively limited memory resources.

To harness the complementary advantages of CPUs and GPUs, this study introduces a heterogeneous computing framework for coupled CFD–DEM simulations that integrates our in-house RTDEM solver with OpenFOAM (v2312). The term *heterogeneous* denotes a strategic memory allocation where all CFD-related data, including mesh, velocity, and pressure fields, reside in CPU memory, while all DEM particle data are stored in GPU memory. During each coupling timestep, CFD and DEM computations execute sequentially on their respective processors (CPU and GPU) and are coordinated through a specialized coupling interface. This interface serves as a critical bridge, enabling bidirectional mapping of DEM particle shapes to the CFD framework while simultaneously transferring updated dynamics from CFD back to DEM.

Fig. 8 illustrates the bidirectional data transfer architecture between the CFD and DEM systems. In this configuration, four CPU processors are exclusively allocated to the CFD solver, while a single GPU handles the DEM solver. The double-headed arrows represent data links connecting CFD memory to DEM memory via the memory bus, which operates using GPU Inter-Processor Communication (IPC) protocols under the coordination of the CFD-DEM coupling scheduler. During each timestep iteration, the coupling scheduler evaluates which memory partitions are ready for computation and which require data fetching. For ready partitions (indicated by the void and blue circle of rank 0), the computational kernel is immediately invoked to advance the simulation, executed by GPU processors in Block A. Simultaneously, for partitions awaiting data (represented by solid circles corresponding to ranks 1-3), the memory bus operates asynchronously with the computational kernel to transfer data between CPU and GPU. This approach effectively overlaps computation with data transfer, eliminating the need for global read-all/write-all operations that would otherwise cause computational idling, particularly in scenarios involving smaller data volumes.

## 4. Benchmark tests

This section presents a comprehensive evaluation of the three solver implementations developed in this study: unresolved, resolved, and

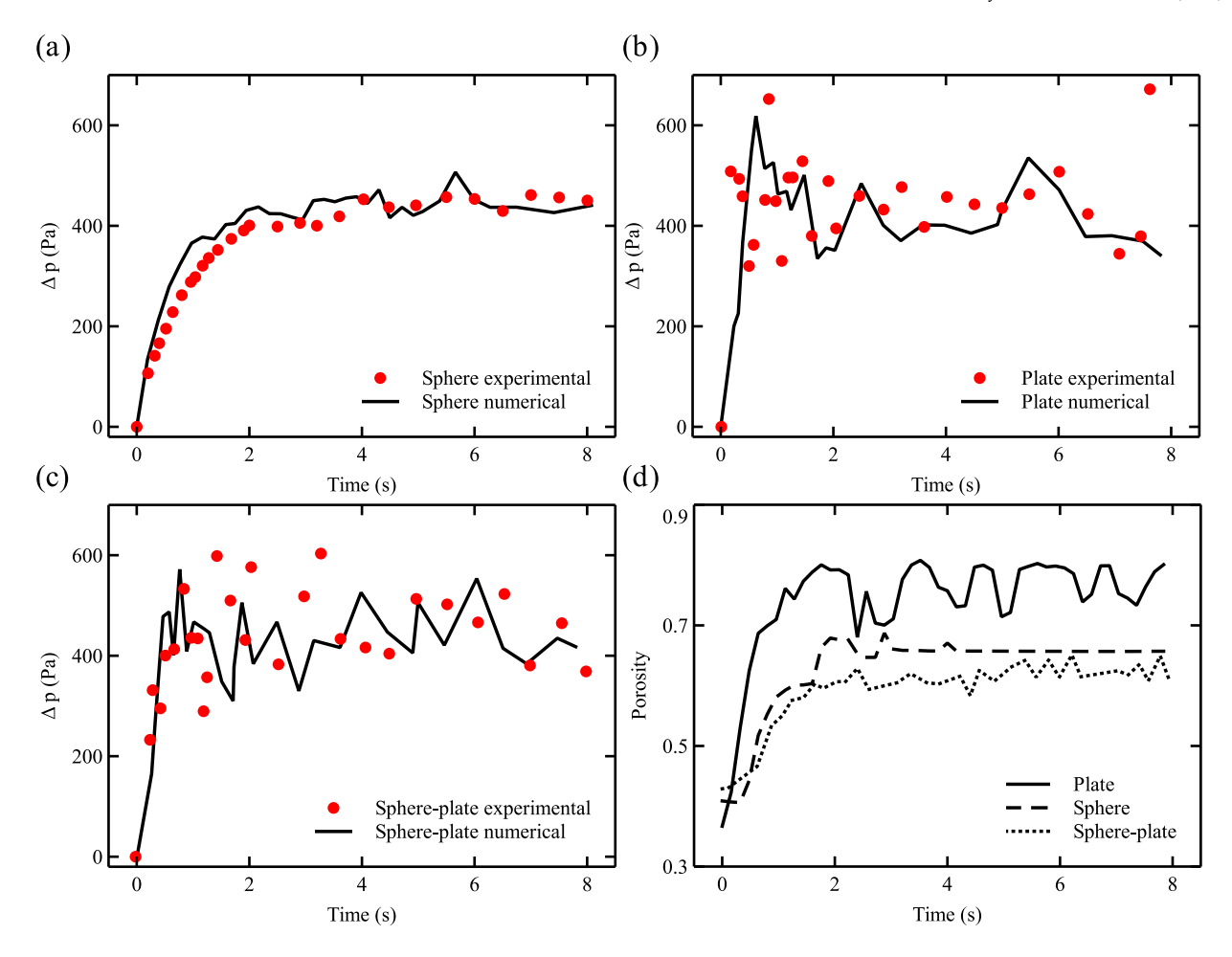


Fig. 12. Pressure drop in the Ergun test for: (a) spheres packing, (b) plates packing, (c) binary packing of spheres and plates, and (d) the evolution of porosity with respect to particle shape.

hybrid CFD-DEM approaches. All benchmark tests and illustrative examples presented throughout the manuscript were performed on a computational server equipped with an Intel Xeon Gold 6248R CPU and an NVIDIA RTX 4090 GPU, ensuring consistent hardware conditions for performance assessment.

## 4.1. Unresolved CFD-DEM

## 4.1.1. Settling of a single sphere

The settling behavior of a single sphere represents a fundamental validation case investigated under two distinct scenarios: Case I examines sphere settling entirely within water, while Case II analyzes sphere transition from air into water. Both scenarios employ drag and buoyancy force models for fluid-particle coupling. Analytical solutions for the critical settling velocities in these configurations have been established in previous studies [72,73]:

$$v_{f1} = \frac{2}{9} \frac{(\rho_p - \rho_w)gR^2}{\mu_w} [1 - \exp(-\frac{9\mu_w t}{2\rho_p R^2})], \tag{12a}$$

$$v_{f2} = \frac{1}{72} \frac{(\rho_p - \rho_w)gR^2}{\mu_w} [1 - \exp(-\frac{4\mu_w t}{27\rho_n R^2})].$$
 (12b)

For the numerical simulations, spheres with radius R=0.5 mm are released from initial heights of 0.5 m and 0.74 m to represent Case I and Case II, respectively, as illustrated in Figs. 9(a, b). The computational domain consists of a water container measuring 0.1 m  $\times$  0.1 m  $\times$  1 m, discretized into 8  $\times$  8  $\times$  80 cells. In Case II, the water–air interface is

established at Z=0.5 m by setting the volume fraction  $\alpha=0$  in all cells above this height. Boundary conditions include no-slip velocity on all walls except the ceiling, which maintains a pressure condition of  $\rho=0$  Pa. The dynamic viscosities are specified as  $\mu_w=1\times 10^{-3}$  Pa s for water and  $\mu_a=1\times 10^{-5}$  Pa s for air, while the densities are  $\rho_p=3,000~{\rm kg/m^3}$  for particles,  $\rho_w=1,000~{\rm kg/m^3}$  for water, and  $\rho_a=1~{\rm kg/m^3}$  for air. The simulation employs a timestep of  $1\times 10^{-3}$  s over a total duration of 15 s.

Figs. 9(c, d) present the comparison between numerical predictions and analytical solutions. The results demonstrate excellent agreement, with the simulated settling velocities for both Case I and Case II closely matching the analytical values, thereby validating the accuracy of the unresolved coupling implementation.

# 4.1.2. Terzaghi's one-dimensional consolidation

Terzaghi's consolidation theory describes the dissipation of excess pore pressure in a one-dimensional porous medium under surcharge loading. According to the fundamental principles established by [74], this process is governed by:

$$\frac{\partial p}{\partial t} = C_v \frac{\partial^2 p}{\partial z^2}.$$
 (13)

where p represents the excess pore pressure, t denotes time, and z indicates the drainage direction (aligned with the vertical axis in this study). The coefficient of consolidation,  $C_v$ , is defined as:

$$C_v = \frac{k_p}{\rho_f g m_v},\tag{14a}$$

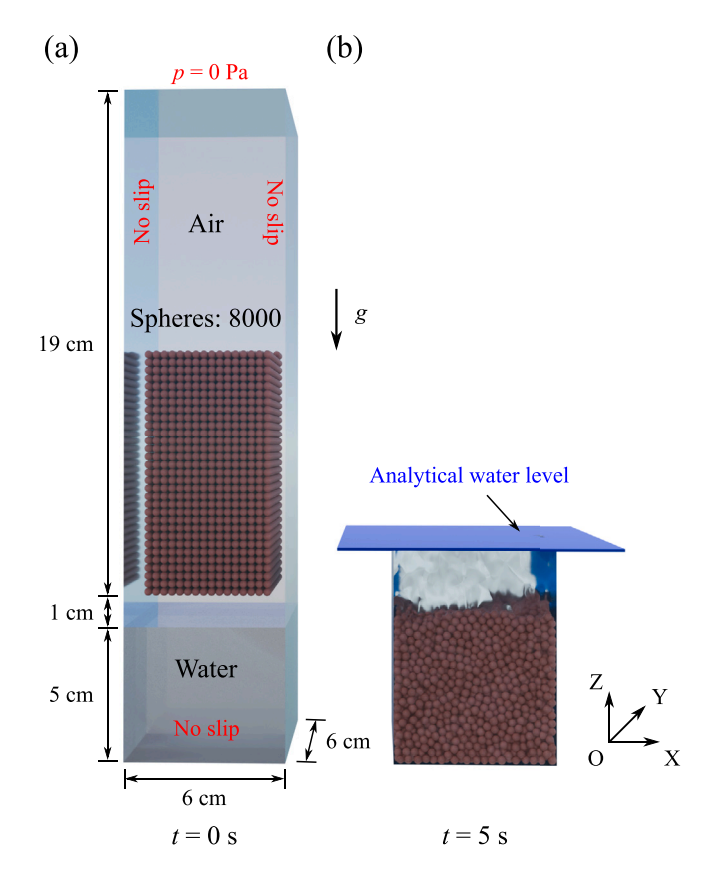


Fig. 13. Entry of multiple spheres into water: (a) schematic diagram of the simulation, (b) final state of the two-phase mixture.

$$T_v = \frac{C_v t}{H^2}. ag{14b}$$

where  $k_p$  represents the material permeability,  $\rho_f$  denotes the fluid density, g is gravitational acceleration,  $m_v$  is the coefficient of volume change,  $T_v$  is the dimensionless time factor, and H is the height of the porous medium column.

Following the methodology proposed by [75], the permeability  $k_p$  and coefficient of volume change  $m_p$  are calculated as:

$$k_p = \frac{D^2 \epsilon_f \rho_f g}{150 \mu_f (1 - \epsilon_f)^2},\tag{15a}$$

$$m_v = \frac{\Delta \epsilon_v}{\Delta \sigma_v},\tag{15b}$$

$$\Delta\epsilon_v = \frac{\delta}{H_0},\tag{15c}$$

$$\Delta\sigma_v = (1 - \epsilon_f)(\rho_p - \rho_f)g\frac{H_0}{2}.$$
 (15d)

where D is the particle diameter,  $\epsilon_f$  is the fluid void fraction,  $\rho_p$  and  $\rho_f$  are the particle and fluid densities, respectively, and  $\mu_f$  is the dynamic fluid viscosity. Moreover,  $\epsilon_v$  represents the volumetric strain of the porous material,  $\delta$  is the vertical displacement of the topmost particle,  $H_0$  is the initial column height, and  $\sigma_v$  is the vertical stress increment.

For a specific column of porous media, as presented in Fig. 10(a), which is subjected to an initial surcharge  $p(z,0)=p_0$ , the boundary conditions include zero pressure at the top p(0,t)=0 and a zero pressure gradient at the bottom given by  $\frac{\partial p}{\partial z}\Big|_{z=H}=0$ . The analytical pressure profile along the coordinate z at a given time  $T_v$  is expressed as follows:

$$p = \sum_{n=1}^{\infty} \frac{2p_0}{n\pi} (1 - \cos n\pi) \sin\left(\frac{n\pi z}{H}\right) \exp\left(-\frac{n^2 \pi^2 T_v}{4}\right). \tag{16}$$

where n denotes the summation index.

The analytical solution for the consolidation settlement  $U_z$  of the porous column, which corresponds to the displacement of the uppermost particle, is expressed as:

$$U_z = 1 - \frac{8}{\pi^2} \sum_{v=-1}^{2n+1, n \to \infty} \frac{1}{m^2} \exp\left(-\frac{m^2 \pi^2 T_v}{4}\right).$$
 (17)

The numerical setup, illustrated in Fig. 10(a), consists of 100 spheres with diameter D=1 mm arranged vertically and fully submerged in fluid. The computational domain is discretized into  $1\times1\times50$  cells. Material properties include particle and fluid densities of  $\rho_p=2,650~{\rm kg/m^3}$  and  $\rho_f=1,000~{\rm kg/m^3}$ , respectively. The linear-spring contact model employs normal and shear stiffnesses of  $k_n=k_s=100~{\rm N/m}$ , while gravitational acceleration is set to  $g=9.8~{\rm m/s^2}$  and fluid dynamic viscosity to  $\mu_f=1\times10^{-3}~{\rm Pa}$  s.

The simulation procedure allows particles to settle under gravity and buoyancy forces until hydrostatic equilibrium is achieved. Subsequently, a surcharge load of  $p_0 = 100$  Pa is applied to the topmost particle. Fig. 10(b) displays the temporal evolution of excess pore pressure profiles as a function of the dimensionless time factor  $T_n$ . The gray line and dots indicate the initial normalized excess pressure of  $\bar{p}_0 = 1$ . The curves progressing from right to left represent the analytical solution, while the dots denote numerical predictions, showing strong agreement between analytical and numerical results except at  $T_v = 0.06$ . Fig. 10(c) presents the settlement of the topmost particle versus  $T_v$ , again demonstrating close alignment with the analytical solution. The minor initial deviation in excess pore pressure stems from limited precision in marker-based void fraction calculation. Following surcharge application, particle-associated markers may cross cell boundaries, introducing numerical discrepancies that would diminish with increased mesh resolution.

# 4.1.3. Ergun test

To evaluate the performance of non-spherical unresolved CFD–DEM coupling, we compare our numerical results with experimental Ergun tests from [76]. The simulation parameters replicate the experimental configuration in a cubic vessel measuring 0.11 m  $\times$  0.11 m  $\times$  0.41 m, as shown in Fig. 11. Initially, particles settle under gravity to form a packing with height 0.1 m, achieving hydrostatic equilibrium. Subsequently, a gradually increasing velocity boundary condition is applied at the bottom wall, reaching a critical velocity of 2.4 m/s over 8 s. This progressive acceleration fluidizes the particle bed, establishing a stable pressure gradient throughout the vessel. Boundary conditions include no-slip walls on the sides and zero pressure at the top. The investigation examines two particle geometries: spheres with radius 0.36 cm and plates with dimensions 0.98 cm  $\times$  0.9 cm  $\times$  0.22 cm. Three packing configurations are considered: pure spheres, pure plates, and a binary mixture, all subjected to drag, pressure gradient, and viscous forces.

Following the experimental protocol, pressure measurements are recorded between elevations Z=0 m and Z=0.3 m. Material properties include particle density  $\rho_p=672~{\rm kg/m^3}$  and air density  $\rho_a=1.168~{\rm kg/m^3}$ , with air dynamic viscosity  $\mu_a=1.832\times 10^{-5}$  Pa s. The linear and shear contact stiffnesses are set to  $k_n=3\times 10^4~{\rm N/m}$  and  $k_s=1\times 10^4~{\rm N/m}$ , respectively. The simulation utilizes a timestep of  $1\times 10^{-4}$  s over a total duration of 8 s.

Figs. 12(a–c) compare pressure drop evolution between numerical predictions (black lines) and experimental measurements (red dots). Both datasets demonstrate a consistent increasing trend that eventually stabilizes. Non-spherical particle cases exhibit more pronounced fluctuations, attributed to rotational motions induced by their asymmetric geometry. These shape effects also influence porosity evolution, as depicted in Fig. 12(d). Following the established relationship between flow direction and particle orientation [36], plate-shaped particles experience stronger fluid-induced forces, resulting in elevated particle beds and reduced porosities. In the binary mixture configuration, where plates segregate above spheres, the void space evolution within the

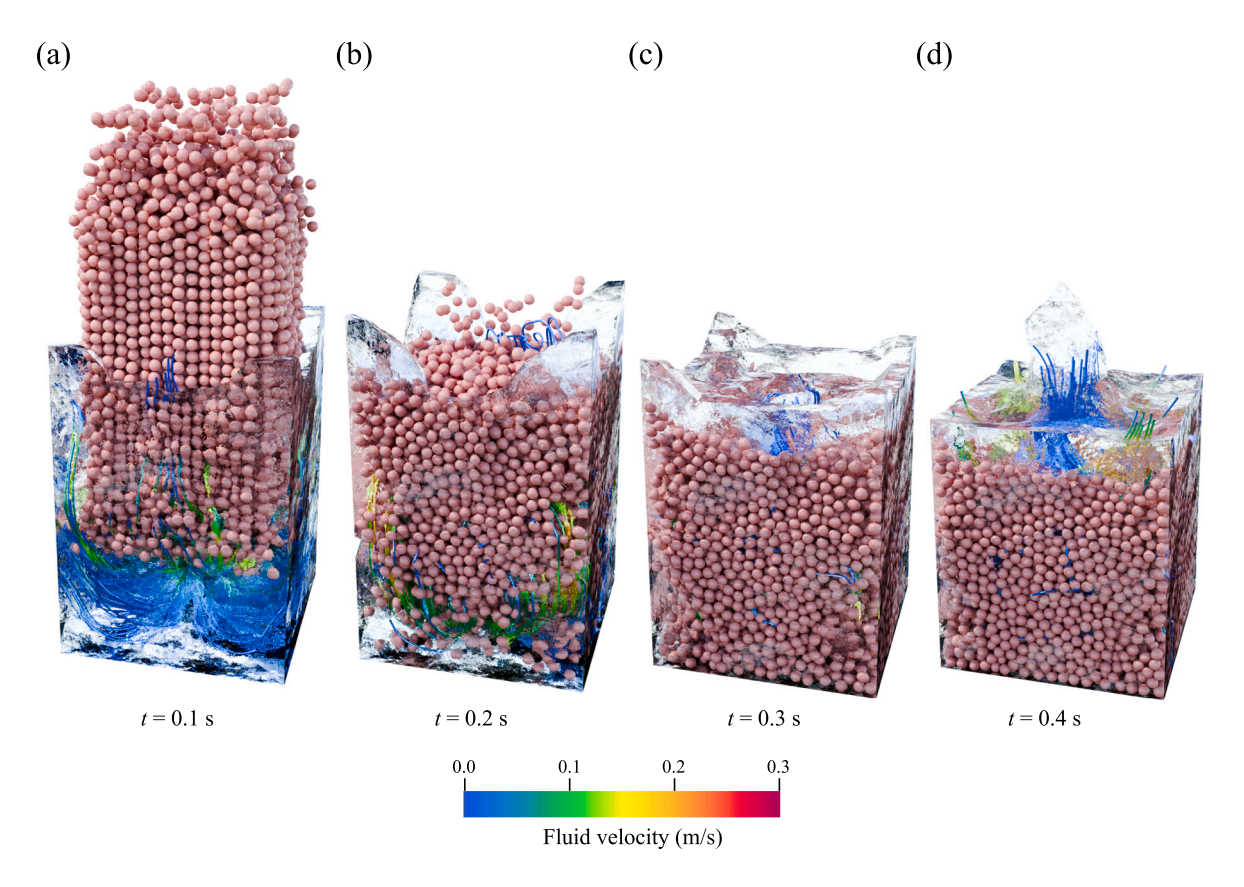
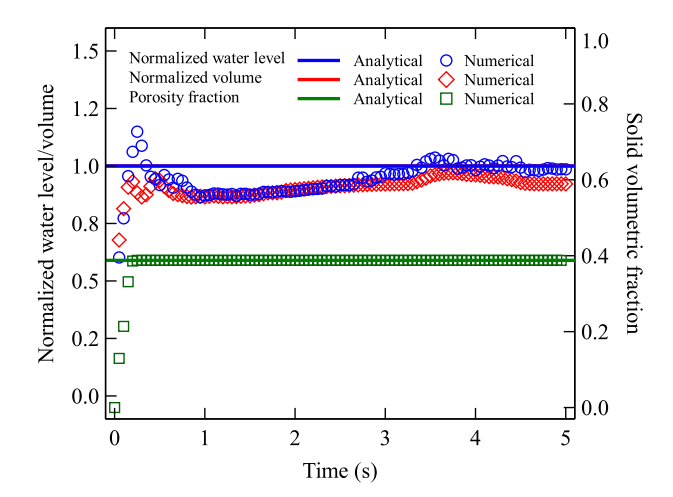


Fig. 14. Snapshots of the entry and settling of multiple spheres.



**Fig. 15.** The comparison between unresolved numerical and analytical results, as defined at steady state, focuses on water level, total volume, and particle volumetric fraction.

spherical region is further modified by the overlying plate particles, yielding lower overall porosity compared to the pure-sphere case.

The computational demands of non-spherical DEM contact detection and particle shape encoding in CFD are substantial. Our implementation achieved a total simulation time of 2.4 h, corresponding to 0.11 s per timestep using 8 CPU cores and 1 GPU. By comparison, an equivalent simulation by Vollmari et al. [76] required several days using 20 CPU cores (Intel EM64T Xeon). This dramatic improvement

demonstrates the significant computational efficiency gains afforded by our unresolved coupling approach.

#### 4.1.4. Settling of a sphere column

This test evaluates the robustness of volume conservation in multisphere fluid systems [77]. Fig. 13(a) presents the simulation configuration in the XOZ cross-section. The computational domain consists of a cubic container measuring 6 cm  $\times$  6 cm  $\times$  25 cm containing 8,000 spherical particles with diameter 3 mm initially arranged in the upper region. The container is discretized into a grid of  $12 \times 12 \times 50$  cells, and it is divided into two distinct regions: the upper region, where air is present ( $Z \ge 5$  cm), and the lower portion, which is filled with water. Boundary conditions include no-slip velocity on all lateral and bottom walls, with zero pressure applied at the top.

Initially, particles fall freely under gravity. Upon water entry, they experience drag and buoyancy forces. Material properties include particle density  $\rho_p=2,500~{\rm kg/m^3}$ , air density  $\rho_a=1~{\rm kg/m^3}$ , and fluid density  $\rho_f=1,000~{\rm kg/m^3}$ . Dynamic viscosities are  $\mu_a=1\times 10^{-5}$  Pa s for air and  $\mu_f=1\times 10^{-3}$  Pa s for fluid. Particle contact mechanics employ normal and shear stiffnesses of  $k_n=8\times 10^3~{\rm N/m}$  and  $k_s=2.4\times 10^3~{\rm N/m}$ , with a friction coefficient of 0.5. The CFD timestep is set to  $2.5\times 10^{-4}$  s for a total simulation duration of 5 s, corresponding to 20,000 timesteps.

Fig. 14 depicts the particle water entry process over the time interval from 0.1 s to 0.4 s. Initially, the water level demonstrates considerable fluctuations, which eventually stabilize by 0.4 s. The final water level recorded at 8.1 cm aligns with the analytical predictions, which take into account the water displacement caused by the particle's intrusion into the initial 5 cm of the water column.

To evaluate volume conservation and porosity within the water-solid mixture, three metrics are monitored (Fig. 15): maximum water level, total water volume, and porosity fraction. Maximum water level is defined as the highest Z coordinate where volume fraction exceeds

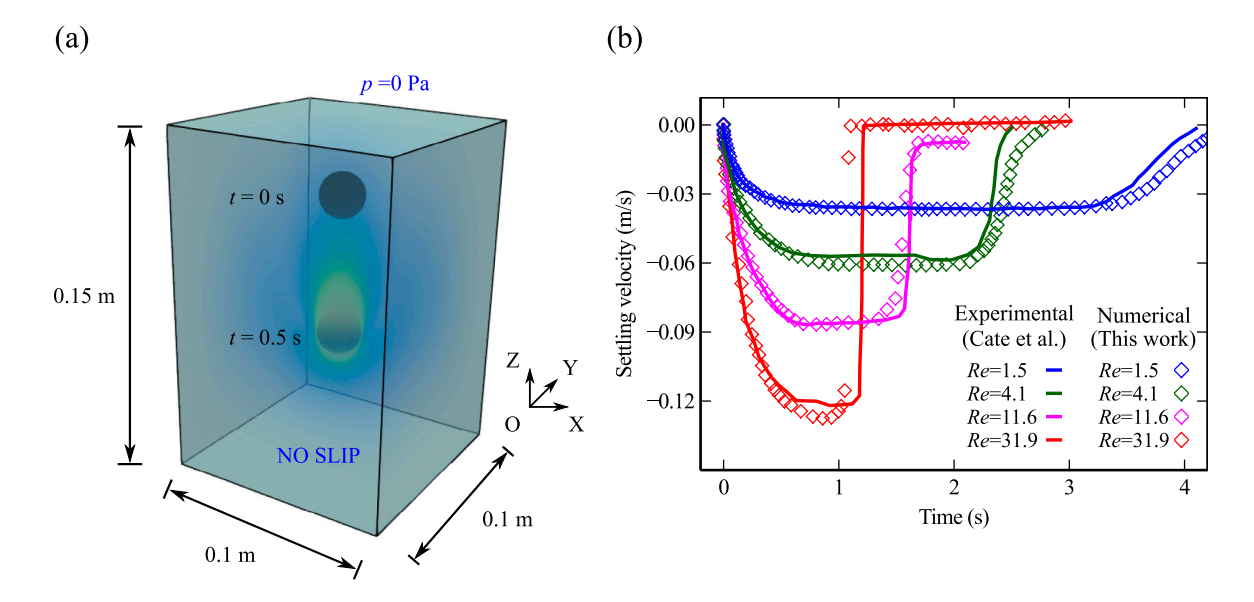


Fig. 16. Entry of a single particle and its collision with a box at varying particle Reynolds numbers: (a) numerical simulation setup, and (b) variation in settling velocity of the particle.

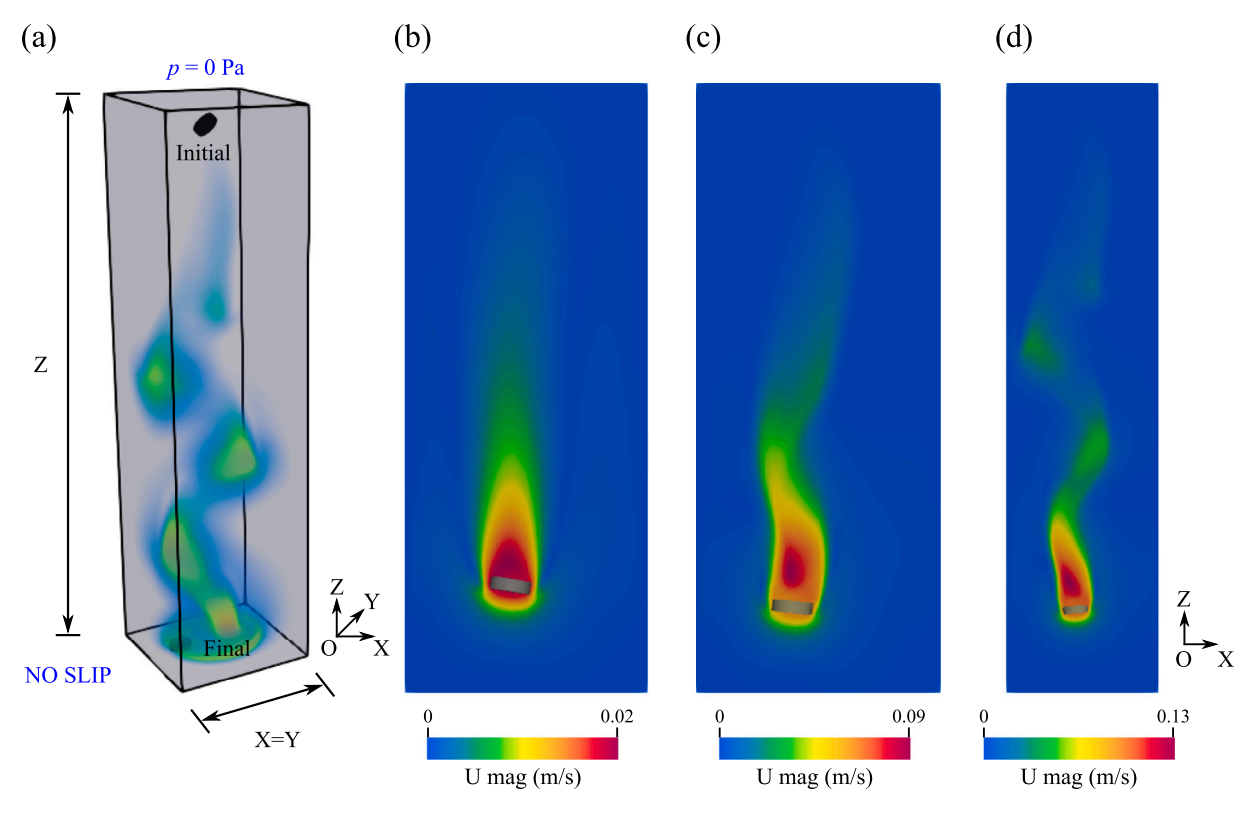


Fig. 17. Settling of the cylinder: (a) initial configuration, followed by snapshots of (b) Group II, (c) Group II, and (d) Group III. Note: The aspect ratio of the snapshots varies as a consequence of the scaling of the fluid domain.

0.99 (tolerance:  $\pm 0.01$ ). Total water volume is computed by summing volumes of cells with volume fraction greater than 0.99. Porosity fraction represents the ratio of particle volume below the stable water level to the total stable volume. The convergence of all three metrics to their analytical solutions confirms the reliability of the unresolved two-phase CFD–DEM method for volume conservation.

## 4.2. Resolved CFD-DEM

# 4.2.1. Settling of spheres

This validation case follows the experimental configurations of [78], illustrated in Fig. 16(a). A sphere with diameter d=0.015 m is centrally positioned within a rectangular box measuring 0.1 m  $\times$  0.1 m  $\times$  0.15 m. The computational domain is discretized into  $80 \times 80 \times 120$  cells. The

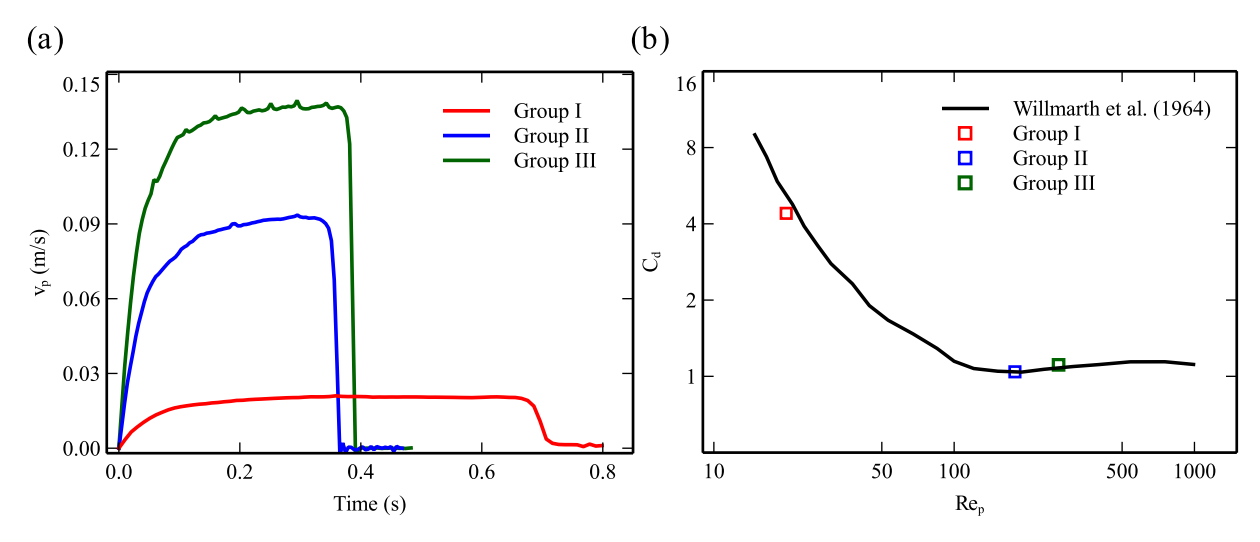


Fig. 18. Velocity of the cylinder as a function of time for (a) Groups I-III, (b) comparison of the drag coefficient obtained in this work with experimental data.

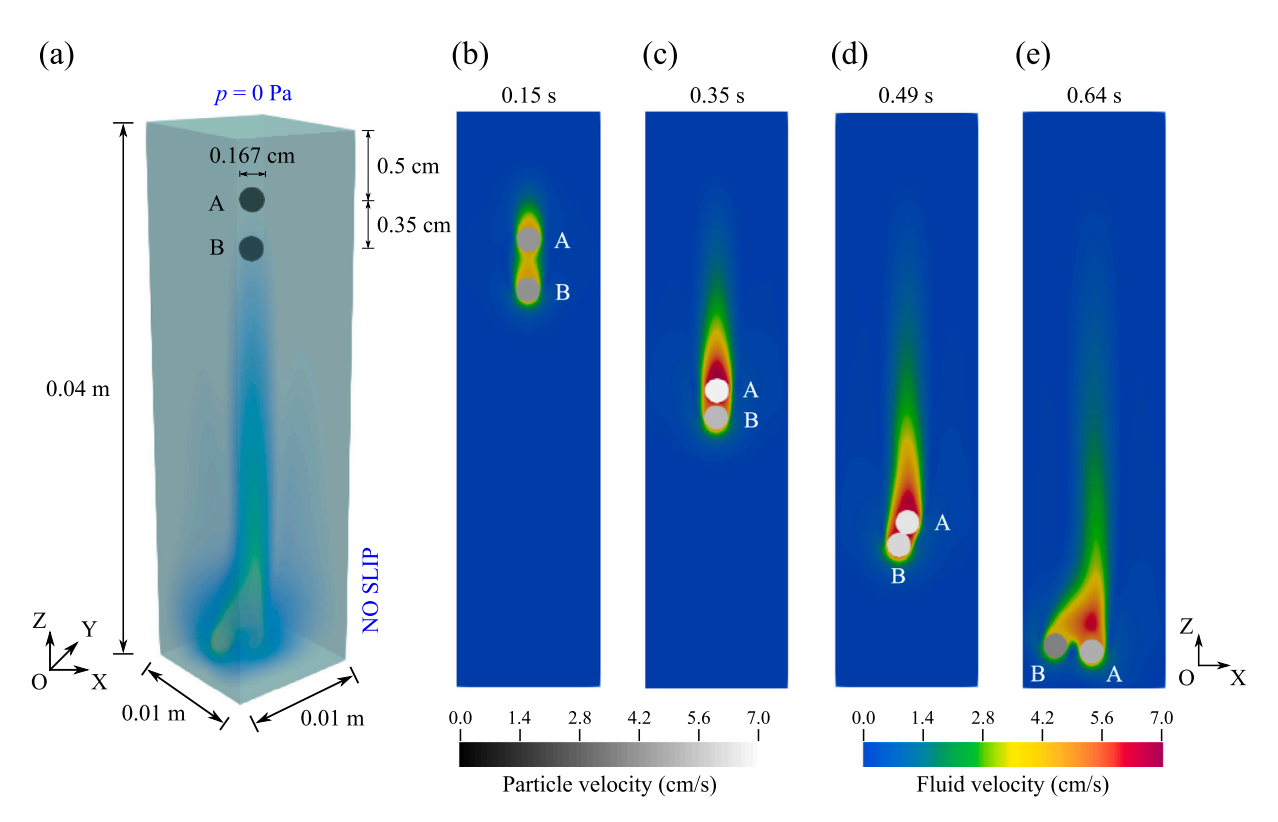


Fig. 19. The (a) numerical simulation setup and (b-e) fluid velocity field contour of DKT for two spheres.

particle density is  $\rho_p=1,120~{\rm kg/m^3}$ . To investigate various particle Reynolds numbers ( $Re_p$ , Eq. (18)), four test cases with different fluid densities ( $\rho_f$ ) and dynamic viscosities ( $\mu_f$ ) are established, as detailed in Table 1:

$$Re_p = \frac{|v_{rel}|d}{v}. (18)$$

where  $|v_{rel}|$  is the relative velocity magnitude between particle and fluid, d is the particle diameter, and v is the fluid kinematic viscosity.

The CFD simulation employs a timestep of  $1\times 10^{-3}$  s and terminates when particles reach the container base under the influence of IB force and buoyancy. Fig. 16(b) compares numerical predictions (markers) with experimental measurements (continuous lines). The numerical results show excellent agreement with experimental data during the settling phase. Minor discrepancies appear during final

 Table 1

 Fluid parameters for the settling-spheres example.

No.	$\rho_f$ (kg/m <sup>3</sup> )	$\mu_f$ (Pa s)	$Re_p$
1	970	0.373	1.5
2	965	0.212	4.1
3	962	0.113	11.6
4	960	0.058	31.9

settling when particles contact the container bottom, potentially due to limitations of the linear-spring DEM contact model in fully capturing particle—container interactions.

# 4.2.2. Settling of cylinders

This validation case replicates the experimental configuration of [79],

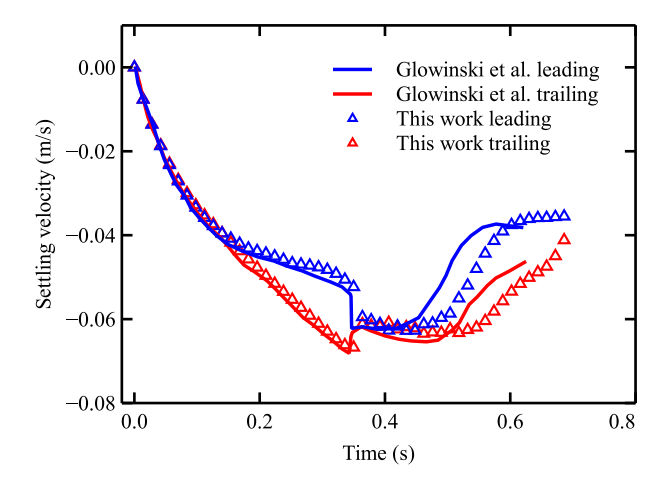


Fig. 20. The settling velocities of leading and trailing spheres in DKT, along with experimental results from the work of [62].

Table 2
Numerical configurations of cylindrical settling.

Group No.	$\rho_p$ (kg/m <sup>3</sup> )	$D_p/H_p$ (mm)	Fluid domain (mm)	$Re_p$
I	1,300	1/0.3	$6 \times 6 \times 15$	20
II	1,750	1/0.3	$6 \times 6 \times 15$	179
III	2,700	2/0.6	$12 \times 12 \times 48$	272

as illustrated in Fig. 17(a). A cylinder is initially positioned near the fluid domain top, rotated 45° about the *Y*-axis, and settles under gravity, IB force, and buoyancy. Following the experimental methodology [79], three test groups are established by varying the fluid domain size and cylinder properties: diameter  $(D_p)$ , height  $(H_p)$ , and density  $(\rho_p)$ , as detailed in Table 2. The corresponding particle Reynolds numbers  $(Re_p)$  are calculated using Eq. (18). Fluid properties include density  $\rho_f = 1,000 \text{ kg/m}^3$  and dynamic viscosity  $\mu_f = 1 \times 10^{-3} \text{ Pa s}$ . The simulation employs a CFD timestep of  $2 \times 10^{-4} \text{ s}$ .

Fig. 18(a) presents the fluid velocity magnitude fields (Figs. 17(b-d)) as the cylinder approaches the bottom (10 units along the Z-axis), along with the corresponding cylinder settling velocities for all three groups. The results demonstrate that fluid velocity initially increases, reaches a plateau, then drops to zero upon cylinder-bottom contact. Group I (lower density) exhibits minimal velocity fluctuations, while Group II (higher density) shows pronounced oscillations, indicating a more dynamic regime. Group III displays the most significant velocity oscillations compared to the relatively stable Group I behavior, suggesting altered settling dynamics. Subsequently, the drag coefficient ( $C_d$ ) is calculated using Eq. (19) and correlated with particle Reynolds number. Fig. 18(b) compares these results with experimental data [79], showing excellent agreement that validates the framework's capability for non-spherical CFD–DEM coupling:

$$C_d = 2 \frac{(\rho_p - \rho_f)}{\rho_f} \frac{|\mathbf{g}| H_p}{|\mathbf{v}_p|}.$$
 (19)

where  $\rho_f$  is the fluid density,  ${\it g}$  is gravitational acceleration, and  ${\it H}_p$  is the cylinder height.

## 4.2.3. Drafting-kissing-tumbling of two spheres

This section investigates the drafting–kissing–tumbling (DKT) phenomenon in a two-sphere system. As shown in Fig. 19(a), spheres A and B are vertically aligned at initial heights of 0.5 m and 0.85 m from the top, respectively. Upon release, the spheres undergo sequential drafting, kissing, and tumbling phases, consistent with experimental observations [80].

The computational domain (0.01 m  $\times$  0.01 m  $\times$  0.04 m) is discretized into  $50 \times 50 \times 200$  cells. The spheres have diameter D = 0.167

cm and density  $\rho_p=1,140~{\rm kg/m^3}$ , while the fluid properties are  $\rho_f=1,000~{\rm kg/m^3}$  and  $\mu_f=1\times10^{-3}~{\rm Pa}$  s. The spheres experience IB force and buoyancy, with the simulation running for 0.7 s using a timestep of  $1\times10^{-3}~{\rm s}$ .

Fig. 20 presents the velocity profiles of the leading particle (B) and trailing particle (A). The trailing particle accelerates more rapidly than the leading particle, exhibiting drafting behavior until approximately 0.35 s. Subsequently, the system enters a kissing phase lasting until 0.49 s, during which numerical results closely match experimental observations. The tumbling phase occurs from 0.49 s to 0.64 s in simulations, earlier than the experimental onset at 0.46 s. Post-tumbling velocities show excellent agreement between numerical and experimental results. The pre-tumbling velocity discrepancies may arise from the linear-spring contact model, which could introduce excessive damping and impede velocity rebound for both particles.

## 4.2.4. Settling of a granular column with arbitrarily-shaped particles

This test validates mass continuity in the coupling framework for arbitrarily shaped particles. As shown in Fig. 21(a), the cubic domain measures 2.6 m  $\times$  2.6 m  $\times$  2.6 m, with air occupying  $Z\geqslant 1$  m and water filling the remaining volume. The computational grid uses  $100\times100\times100$  cells. In the air region, 2,560 non-spherical particles are uniformly distributed in a  $16\times16\times10$  arrangement. Material properties match those in Section 4.1.4, except for the STL particle equivalent diameter of 0.1 m. Complete particle submersion raises the water level by approximately 0.198 m, as indicated by the blue plate in Fig. 21(b).

The simulation uses CFD and DEM timesteps of  $1\times10^{-4}$  s and  $1\times10^{-5}$  s, respectively, for a total duration of 0.5 s. During the first 0.25 s, particles undergo multiple phases: water surface contact, IB force and buoyancy effects, subsequent impacts, energy dissipation, and eventual stabilization into a static regime, as illustrated in Figs. 21(c-f).

Fig. 22 presents the maximum water level, total water–particle system volume, and porosity evolution. Unlike the unresolved case (Fig. 15), the resolved approach shows initial increase followed by decrease in water level and total volume, eventually stabilizing with minimal fluctuations. The numerical results align closely with three analytical benchmarks: expected water level for fully merged particles, total fluid and particle volumes, and terminal particle volume fraction below the initial water level. These results demonstrate the effectiveness of volumetric particle representation for complex geometries in CFD, enabled by the marching-cube-like algorithm for volume fraction calculation.

We benchmark our framework against OpenHFDIB [81], a CPU-parallel arbitrary-shape resolved CFD–DEM implementation. Our CFD domain contains 1 million cells versus OpenHFDIB's 3 million cells, while our DEM case uses 2,560 STL particles compared to OpenHFDIB's 3,000 particles. OpenHFDIB reports 8.7–17.3 s per timestep on 32 and 8 CPU cores (AMD EPYC 7551), respectively. Our framework achieves 3.2 s per timestep using 8 CPU cores with one GPU. The normalized performance of our solver approximates OpenHFDIB on 32 CPU cores, demonstrating the potential to offload CFD–DEM coupling workload to GPU and alleviate CPU bottlenecks in core-limited systems.

# 4.3. Hybrid CFD-DEM: Turbulent flow over a rough bed

The final benchmark validates hybrid CFD–DEM coupling for turbulent flow over a rough bed in an open-channel configuration. Following the experimental setup of Grass et al. [82], as shown in Fig. 23, the reference length is d=1 cm. The computational domain measures  $6d\times 4d\times 1d$ , discretized into  $240\times 160\times 40$  CFD cells. A total of 6,635 spheres with diameter  $D_p=0.001$  m are randomly packed at the domain base under gravity and buoyancy forces.

Boundary conditions include slip at the top surface, no-slip at the bottom, and periodic conditions on lateral walls for CFD. For DEM, the top and lateral walls are non-periodic, with periodicity only along channel side walls. Particle and fluid densities are  $2,650 \text{ kg/m}^3$  and

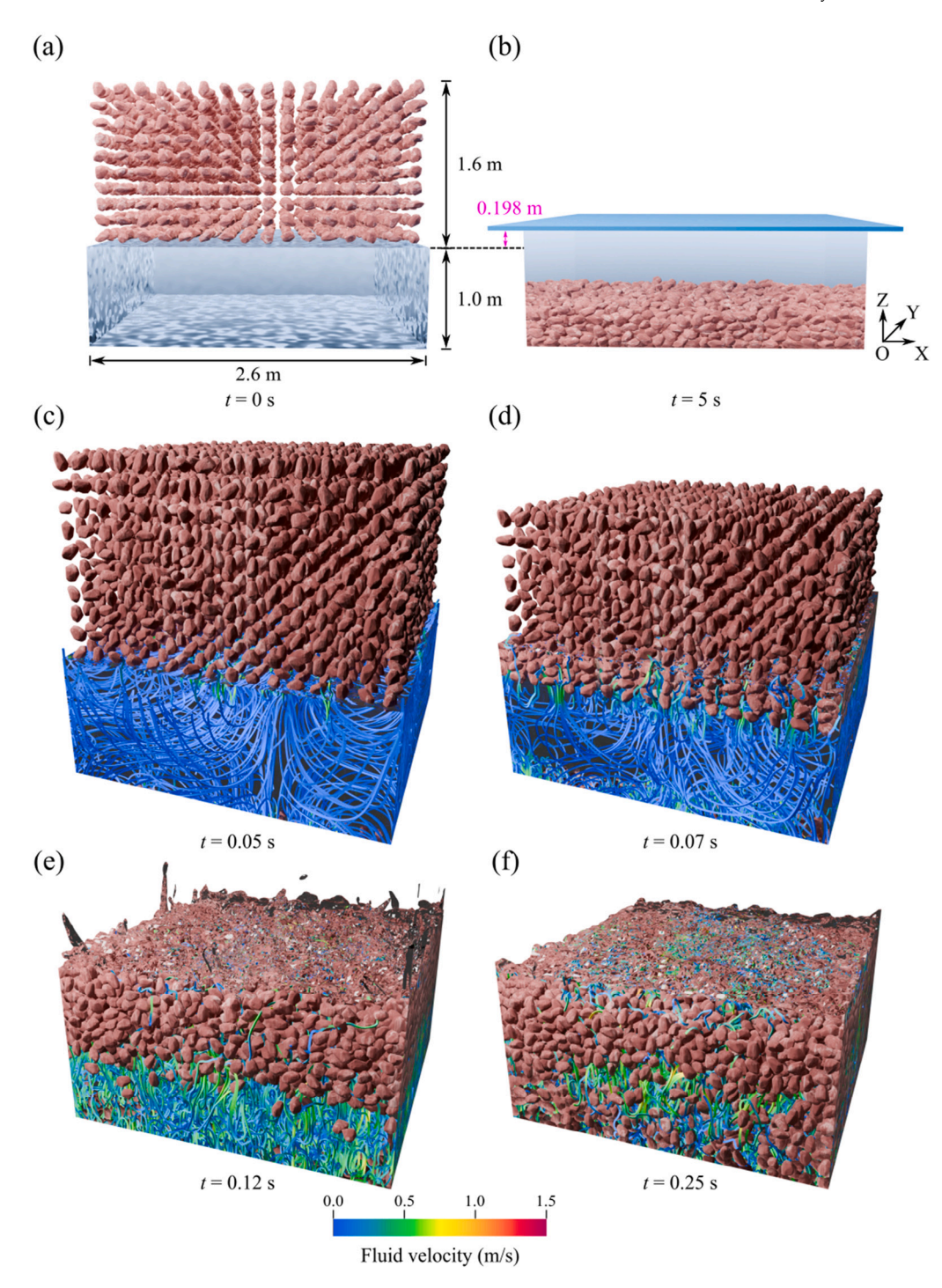


Fig. 21. Entry of STL-encoding non-spherical particles into water: (a-b) the initial and final states, and (c-f) snapshots of the particles falling into the water.

1,000 kg/m³, respectively. Flow is driven by body force  $b_x=U_\tau^2/d$  with friction velocity  $U_\tau=0.03$  m/s. The roughness Reynolds number  $k_s^+=79$  (Eq. (20)) maintains fully developed rough flow near the laminar–turbulence transition threshold (approximately 70), following Ligrani and Moffat [83].

$$k_s^+ = \frac{k_s U_\tau}{v} \tag{20a}$$

$$k_s = \beta d \tag{20b}$$

where  $k_s$  is particle-equivalent roughness and  $\nu=1\times 10^{-6}~{\rm m}^2/{\rm s}$  is fluid kinematic viscosity. Following Singh et al. [84],  $\beta=0.242$ 

links particle roughness to reference channel length under identical numerical settings.

To evaluate the hybrid solver's applicability to turbulent flows, particles are randomly assigned resolved (blue) and unresolved (red) modes, as shown in Fig. 23(a). The particle-to-cell size ratio of approximately 4:1 requires specialized handling for unresolved particles. High-resolution decomposition markers are defined specifically for unresolved particles, which can span up to four fluid cells per axis and potentially engulf entire cells. A minimum void fraction threshold of 0.1 in unresolved regions mitigates abrupt variations and numerical oscillations.

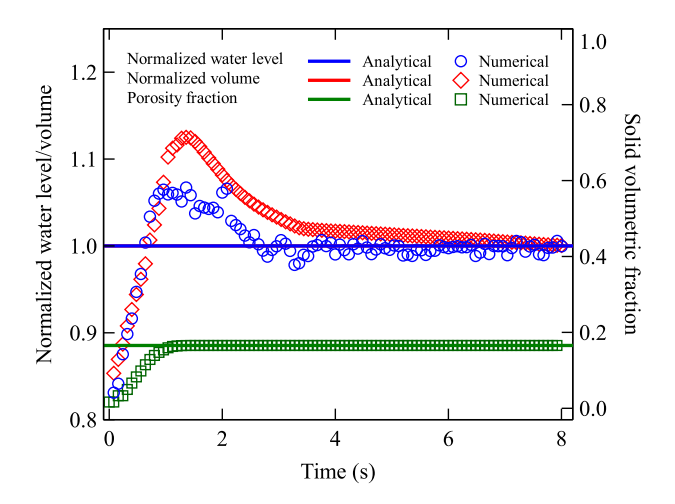


Fig. 22. Water level evolution and particle packing fraction of resolved-coupling water entry of non-spherical particles.

This approach enables the hybrid solver to function as a semi-unresolved/resolved coupling framework for monodisperse systems. CFD and DEM timesteps are  $5\times 10^{-5}$  s and  $5\times 10^{-7}$  s, respectively (100 DEM substeps per CFD step), for total simulated time of 3 s. Fig. 23(b) shows the velocity profile at Y=2 cm slice, while Fig. 23(c) presents X-direction-averaged normalized velocity. Results show good agreement with Grass et al. [82] experimental data. Residual deviations stem primarily from CFD modeling differences: Grass et al. used Large Eddy Simulation (LES), while our solver employs laminar Navier–Stokes approximation for turbulent effects. Given the transitional roughness Reynolds number regime, partial under-resolution of Kolmogorov scales likely contributes to discrepancies, particularly in regions distant from the particle bed.

In conclusion, this benchmark demonstrates the hybrid CFD-DEM solver's suitability for transitional laminar-turbulent flows, with extension to fully developed turbulent flows identified as an important direction for future research.

# 5. Examples: Fluid-driven clogging in granular materials

Fluid-driven clogging [85,86] is prevalent in natural and industrial systems. Unlike gravity-driven clogging, fluid-driven clogging involves complex particle–fluid interactions manifesting in two modes: superficial and internal. Superficial clogging occurs when fine particles accumulate on coarse scaffold surfaces, forming a distinct interface between pore and fluid regions. Internal clogging involves fine particles trapped within the coarse material's internal pore network, creating anisotropic flow heterogeneity. The latter requires particle-scale interaction analysis, favoring resolved coupling schemes, while superficial clogging is better suited to unresolved approaches.

This section demonstrates our hybrid CFD–DEM solver's versatility for fluid-driven clogging challenges. We first simulate superficial clogging using the unresolved scheme to validate robustness with large populations of fine, irregular particles. Then, internal clogging is investigated using both fully resolved and hybrid approaches. These case studies illustrate how the hybrid framework achieves superior balance between computational accuracy and efficiency compared to pure resolved schemes.

#### 5.1. Superficial clogging

As shown in Figs. 24(a, b), the simulation domain (0.06 m  $\times$  0.06 m  $\times$  0.3 m) contains two particle groups: fine and coarse. Fine particles have diameters  $D_f=1$  mm and  $D_f=0.6$  mm, while coarse

**Table 3**Numerical settings of particle shape, size and number.

Particle shape (coarse/fine)	Size ratio	Coarse number	Fine number
non-sphere/sphere	1:3	10,000	20,000
non-sphere/sphere	1:5	10,000	92,592
non-sphere/non-sphere	1:3	10,000	20,000
non-sphere/non-sphere	1:5	10,000	92,592

particles have equivalent diameter  $D_c=3$  mm, forming 1:3 and 1:5 size ratios. Initially, coarse particles are compacted at the domain bottom to 0.092 m height, while fine particles are randomly distributed in the upper region ( $Z\in(0.1,0.3)$  m). A pressure gradient (50 kPa top, 0 kPa bottom) drives fine particle downward migration through the coarse layer. Four test groups are established by varying particle shapes between spherical and non-spherical forms (Table 3).

All particles have density 2,650 kg/m³. Fine particles use normal and tangential stiffnesses of 1,500 N/m and 750 N/m, while coarse particles employ  $1 \times 10^6$  N/m and  $5 \times 10^5$  N/m, respectively. Interparticle friction is 0.2 with damping of 0.3. The CFD mesh resolution is  $15 \times 15 \times 76$  cells. Water properties include density 1,000 kg/m³ and dynamic viscosity  $1 \times 10^{-3}$  Pa s. Timesteps are  $1 \times 10^{-5}$  s (CFD) and  $1 \times 10^{-7}$  s (DEM). Simulation terminates when average particle kinetic energy falls below  $10^{-7}$  J [87].

Cake formation development, characterized by accumulated fine particle ratio in the final cake, is shown in Figs. 24(c) and 25 versus normalized time  $(t/t_{max})$ . Size ratio 1:3 groups show consistent cake formation regardless of particle shape, while 1:5 groups diverge with non-spherical specimens forming cakes earlier than spherical ones. Coarse base particles in 1:3 groups enhance clogging, accelerating cake formation. In 1:5 groups, fine particle penetration occurs alongside cake formation, delaying effects compared to 1:3 groups. Reduced interlocking in spherical 1:5 groups enables greater fine particle penetration, causing the most significant cake formation delay.

The results depicted in Fig. 26 clearly illustrate the unique characteristics of filter cake formation observed across the four sub-tests at their final states. Fine particles with a size ratio of 1:5 produced a broad distribution, spanning from the bottom to the top of the coarse particle packing. In contrast, fine particles with a 1:3 size ratio primarily formed filter cakes on the uppermost layer of the coarse particle domain, as evidenced by comparisons between the first and second rows and between the third and fourth rows.

Fig. 27 presents porosity and pressure variations along the Z-direction for all four test cases, with values surface-averaged at each height. From Z=0 to 0.06 m, porosity trends collapse across size ratios, showing spheres pack more loosely than non-spherical particles at the domain base regardless of size. Beyond 0.06 m, porosity peaks at 0.07 m before declining at 0.08 m due to cross-sectional area variations in the averaging region. For  $Z \ge 0.08$  m, a transition zone shows linear porosity increase toward unity, indicating granular-fluid convergence. Non-spherical samples overlap closely at both size ratios, while spherical samples diverge more, suggesting sphere size variation (1:3 vs 1:5) significantly affects cake formation blockage.

Pressure development contrasts with porosity patterns. In the lower domain, pressure shows size dependence (1:3 ratio > 1:5 ratio), while porosity exhibits shape dependence (spheres > non-spheres). Near the transition zone, trends shift: spherical pressure curves converge while non-spherical curves approach but do not merge, indicating transition from size- to shape-dependent behavior. During filtration, non-spherical particles pack denser than spheres, enhancing interlocking and reducing porosity variations. However, particle orientation significantly affects pressure distribution, creating larger pressure differentials between spherical and non-spherical samples by simulation end.

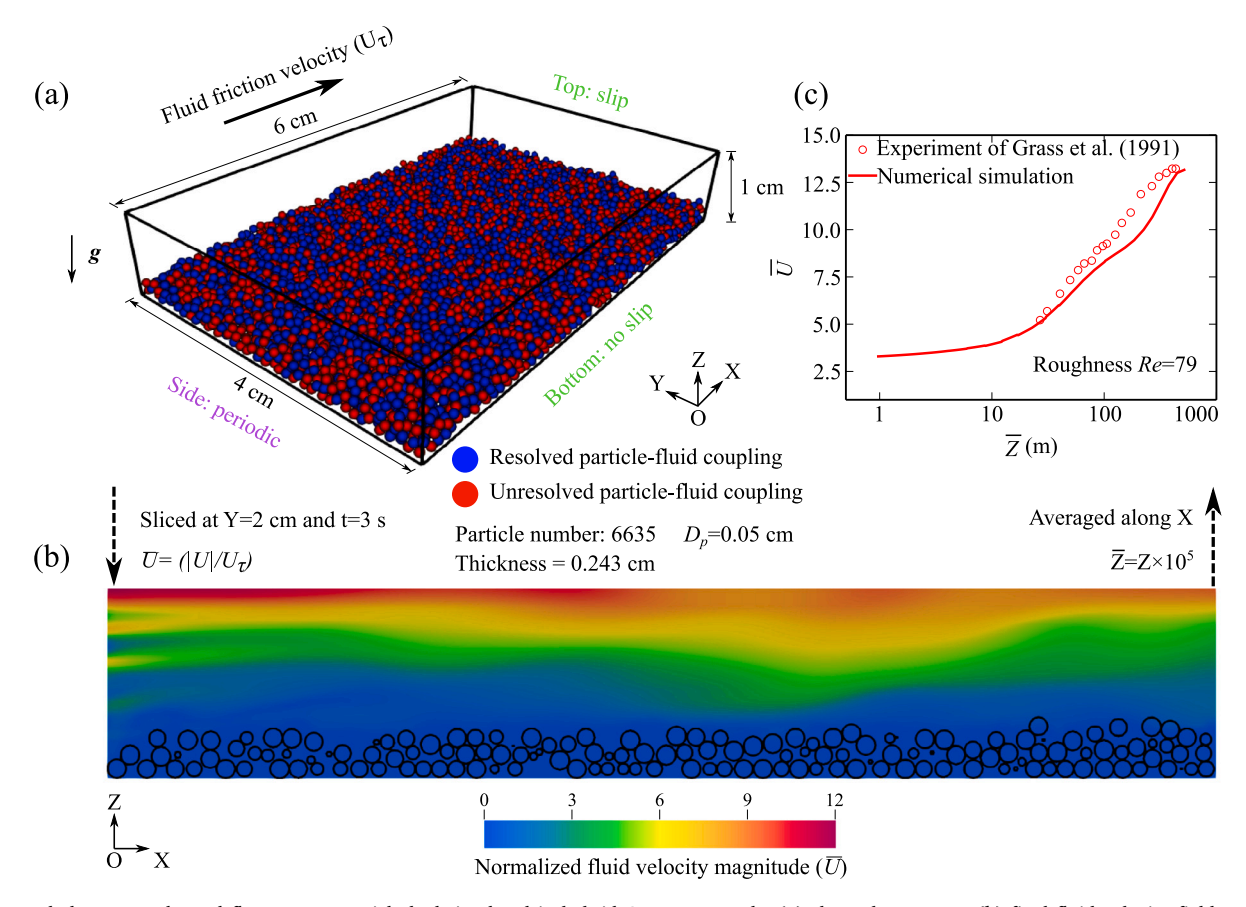


Fig. 23. Turbulent open-channel flow over a particle bed simulated in hybrid CFD-DEM mode: (a) channel geometry, (b) final fluid velocity field and particle configuration, and (c) normalized fluid velocity profile as a function of the normalized Z-coordinate.

**Table 4**Basic parameters for the internal clogging simulation settings.

Parameter	Value	
Particle density $\rho_p$ , kg/m <sup>3</sup>	2,650	
Elastic modulus $\stackrel{.}{E}$ , Pa	$1 \times 10^{9}$	
Poisson's ratio v,	0.3	
Inter-particle coefficient of friction $\mu_p$	0.3	
Fluid density $\rho_f$ , kg/m <sup>3</sup>	1,000	
Fluid dynamic viscosity $\mu_f$ , Pa s	0.001	

#### 5.2. Internal clogging

## 5.2.1. Basic model setup

Gap-graded material clogging in fluid flow is simulated using fully resolved or hybrid resolved–unresolved CFD–DEM approaches. Particles are randomly packed in a 3 cm  $\times$  3 cm  $\times$  5 cm cubic domain (Fig. 28(a)). After equilibrium, inlet velocity  $v_0=0.1~\rm m/s$  is applied at the bottom wall with a sieve at  $Z=4~\rm cm$  to induce clogging. Upper walls maintain zero pressure. Two gap-size configurations are evaluated: coarse spheres with fine non-spherical particles (Fig. 28(a), termed "coarse sphere" group) and coarse non-spherical with fine non-spherical particles (Fig. 28(b), termed "coarse non-sphere" group). Coarse particles have equivalent diameter 6 mm, fine particles 1.2 mm. Both coarse and fine non-spherical particles share identical geometry. Total particle counts are 130 coarse and 7,400 fine particles.

The simulation parameters are set in Table 4. The CFD and DEM simulations are executed with time steps of  $5\times10^{-5}$  s and  $5\times10^{-7}$  s, respectively, culminating in a total simulation duration of 2 s across 40,000 CFD iterations.

## 5.2.2. Fully resolved simulation

The CFD simulation domain is discretized into a grid of  $74 \times 74 \times 118$  cells, which guarantees that the dimension of the fine particles are sufficiently larger than the cells sizes, thereby satisfying the fully resolved conditions for both particle types.

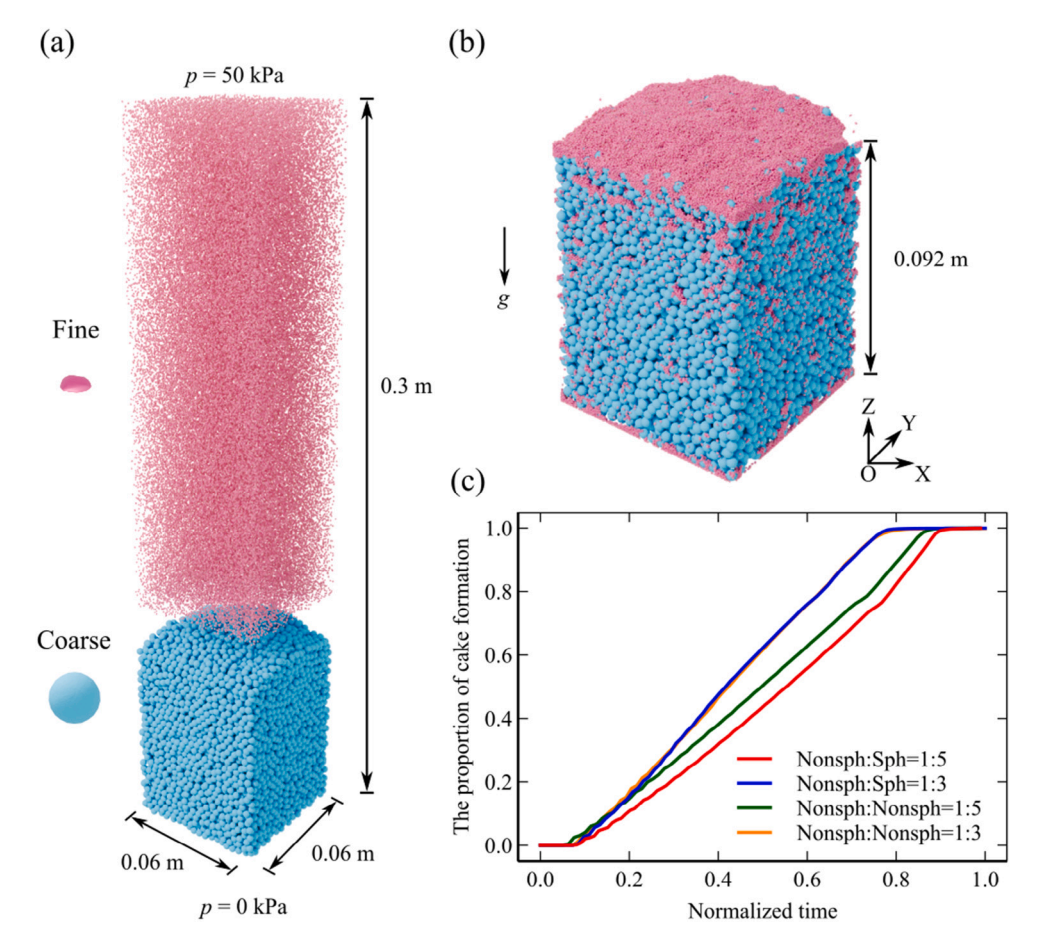
Fig. 29 shows temporal evolution of the particle system. The top row displays coarse sphere/fine non-sphere behavior, while the bottom row shows coarse non-sphere/fine non-sphere dynamics. Both configurations develop binary distributions, forming void-space separators between upper and lower segments. Eventually, larger particles accumulate near the sieve, creating clogs. The non-spherical group exhibits stronger clogging than the spherical group, evidenced by thicker granule layers passing through the sieve at t = 2.0 s.

Fig. 30 shows fine particles beginning sieve passage at 0.25 s (spherical) and 0.35 s (non-spherical). The spherical group has steeper passage rate, achieving 32% throughput versus 16% for non-spherical. Fig. 31 (top row) presents averaged fine particle velocity  $(v_p)$  profiles along Z-direction, revealing sequential peaks and clogs: high-velocity inlet region (Peak A), stationary clog (Clog A), secondary flow surge (Peak B), second stationary clog (Clog B), and uniform post-sieve flow (Peak C).

Contrasting particle velocity trajectories, Fig. 31 (bottom row) shows pronounced pressure drops where particle movement is impeded, particularly at Clog B. This observation aligns with literature reports of similar pressure profiles [88]. Results were validated against the Ergun equation [89]:

$$\frac{\Delta p}{L} = 150 \frac{\mu_f |U_f|}{D_p^2} \frac{(1 - \epsilon)^2}{\epsilon^3} + 1.75 \frac{\rho_f |U_f|^2}{D_p} \frac{(1 - \epsilon)}{\epsilon^3}.$$
 (21)

where pressure gradient  $\Delta p/L$  depends on fluid dynamic viscosity  $\mu_f$ , superficial inlet velocity  $U_f$ , fluid density  $\rho_f$ , fluid volume fraction  $\epsilon$ , and particle diameter  $D_p$ .



**Fig. 24.** The modeling of the superficial clogging tests includes: (a) particle generation, (b) the filter cake at the final stage, and (c) the growth of the cake as a function of normalized time  $(t/t_{max})$ .

At each time instance, clogging regions are identified by pressure curve slope evaluation between zero-slope endpoints. Fluid volume fraction and volume-weighted average equivalent diameter of coarse-fine mixtures are collected to calculate pressure gradients. Numerical pressure gradients (colored markers) are compared with Ergun equation predictions (black lines) in Fig. 31 inset, showing strong agreement for both spherical and non-spherical particle groups.

For spherical particles, pressure stabilizes below Clog B, while non-spherical particles show stabilization at and above Clog B. This discrepancy stems from interlocking behavior: irregular particles form more stable clog structures than spheres, enabling pressure stabilization above Clog B. Below Clog B, non-spherical particles lack established force chains and their anisotropic shapes impede pressure stabilization through fluid dynamics effects.

Fig. 32 shows fluid velocity snapshots in the XOZ-plane at Y=1.5 cm. Both groups exhibit initial inlet-driven flow peak (A) at 0.1 s. The sphere group shows separation, transient clogging ( $\sim$ 0.5 s), and eventual clog breakdown. The non-sphere group follows similar sequence but with longer clogging duration ( $\sim$ 1 s). Poor sphere interlocking enables rapid clog degradation into open channels, allowing fine particles through the sieve, shown by pressure increase in Fig. 31(a). Stronger non-spherical interlocking delays pressure increase until 1.5–2.0 s (yellow/green curves, Z=0.035-0.040 m in Fig. 31(b)). Both groups indicate clog breakdown induces fluid squeezing, causing local velocity and pressure elevation.

Compared to Liu et al. [90] benchmark (0.5 million CFD cells, 2,144 STL particles), our study uses 0.6 million CFD cells and 7,530 STL particles. Their computational time is 74.8 s/timestep on 32 Intel Xeon E5-2680 v4 CPU cores, while our framework achieves 3.61 s/timestep using only 8 CPU cores with one GPU. This demonstrates substantial performance improvement for practical resolved CFD–DEM simulations.

## 5.2.3. Hybrid resolved-unresolved simulation

This section utilizes a grid of  $22 \times 22 \times 40$  cells, which is approximately 33 times coarser than the fully resolved simulation presented in Section 5.2.2. This coarse grid configuration allows for resolved coupling of coarse particles, while fine particles are modeled using an unresolved approach.

Fig. 33 compares particle passage and pressure evolution between resolved and hybrid simulations. Hybrid simulations show 100% particle passage plateau between  $Z=0.04~\mathrm{m}$  and  $Z=0.05~\mathrm{m}$  for both groups, indicating minimal sieve passage. A second plateau ( $Z=0.01~\mathrm{m}$  to  $Z=0.02~\mathrm{m}$ ) is more pronounced in hybrid simulations, suggesting stronger bimodal distribution than resolved cases.

Both simulations show decreasing particle passage over time, while pressure exhibits opposing trends, especially for non-spherical cases. Hybrid simulation shows substantial pressure increase versus minimal increase in resolved simulation (Fig. 33(d)). As discussed in Section 5.2.2, particle structure squeezing can lead to increased fluid pressure, as well as higher fluid velocity at the cross-section of the hybrid configuration, as shown in Fig. 34. It can be inferred that sparsely distributed flow channels persist within the clogging regions, indicating that hybrid coupling exhibits more pronounced squeezing effects at elevated velocities. Unlike fully open channels observed in resolved simulation, hybrid channels facilitate a more significant particle blockage effect.

Despite similar squeezing effects, normalizing converged pressure by plateau values (Figs. 33(c-d)) shows consistent trends across both scenarios. Averaged particle velocity along Z-direction reveals similar two-peaked distributions in hybrid and resolved simulations, with peaks at nearly identical positions.

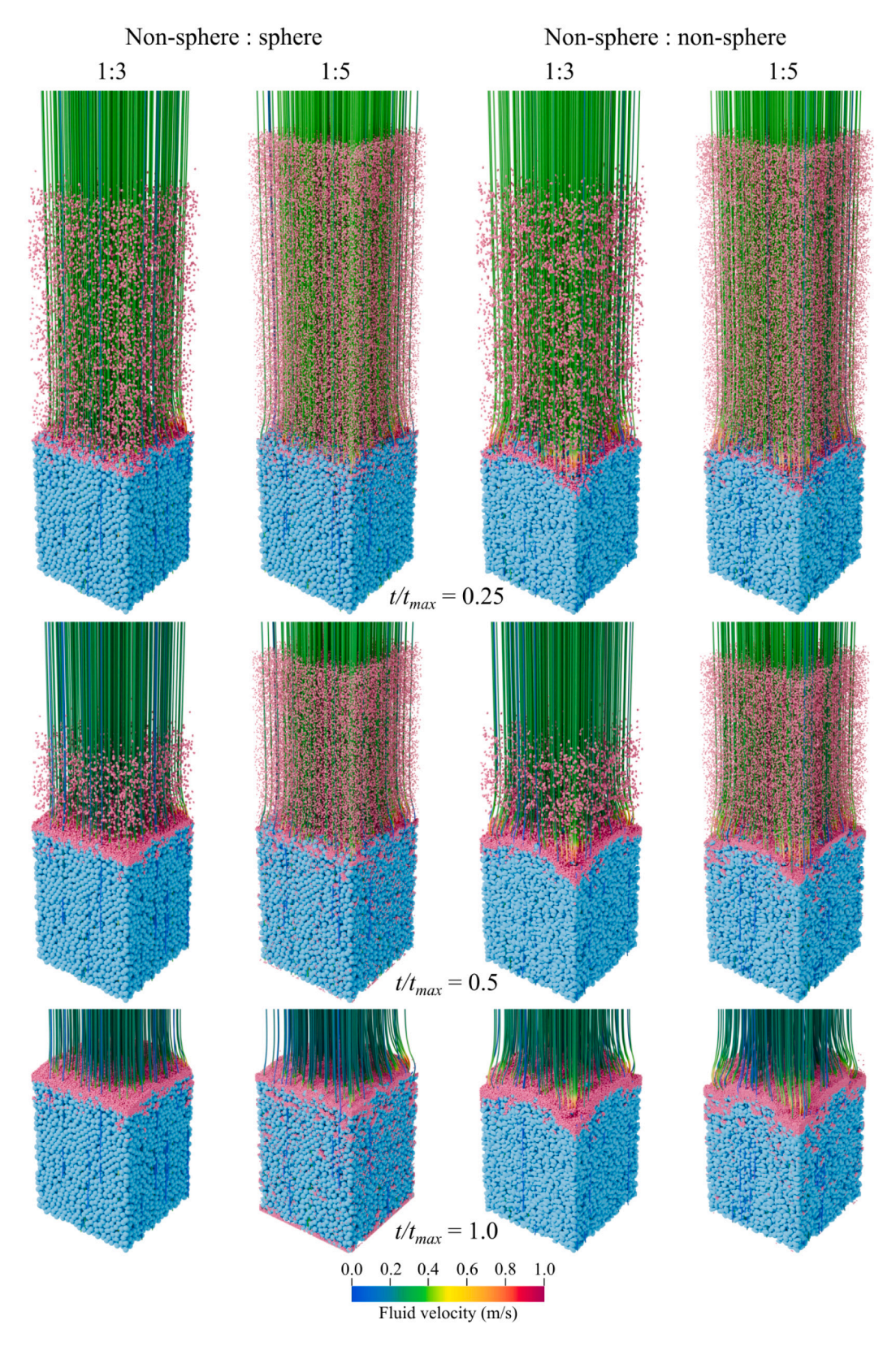


Fig. 25. Snapshots of superficial clogging at different normalized time instants.

To evaluate accuracy–efficiency trade-offs, Figs. 35(a,b) show time-averaged particle velocity  $(v_p)$  and fluid pressure (p) along Z-direction. Hybrid (markers) and resolved (lines) simulations are compared. The hybrid method effectively captures particle velocity profiles with quantitative and qualitative agreement, particularly in peak positions and

plateaus. Normalized particle velocity differences ( $|v_p|/v_{p,max}$ ) remain within 0.4 regardless of particle shape (Fig. 35(c)). Fluid pressure differs substantially: hybrid yields ~3× greater pressure than resolved simulations ( $|p|/p_{max}$ , Fig. 35(d)). Despite magnitude differences, hybrid pressure trends resemble resolved simulations. Normalized pressure

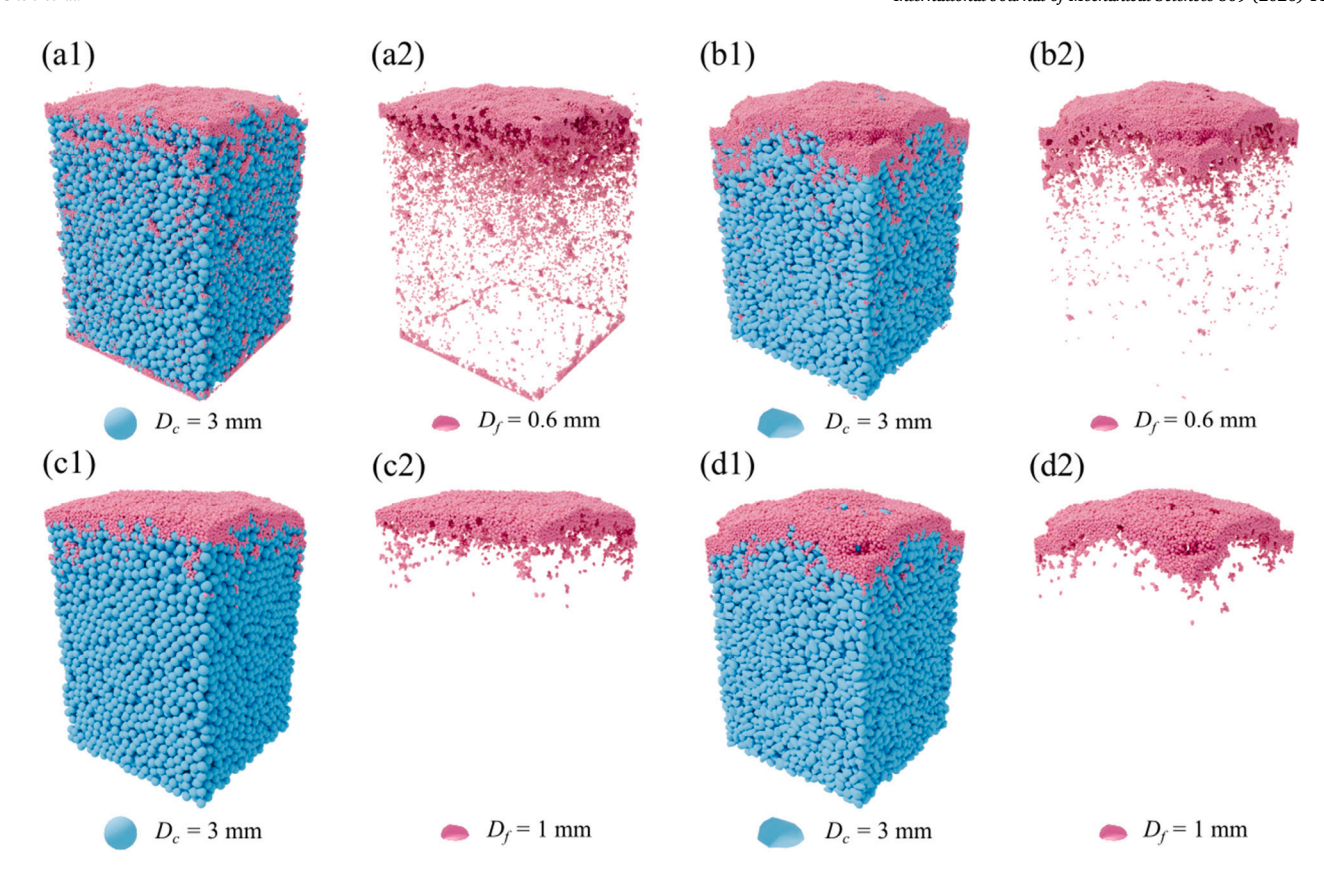


Fig. 26. Snapshot of the final states for the four sub-tests in superficial clogging: (a) size ratio 1:5 with spherical coarse particles; (b) size ratio 1:5 with non-spherical coarse particles; (c) size ratio 1:3 with spherical coarse particles.

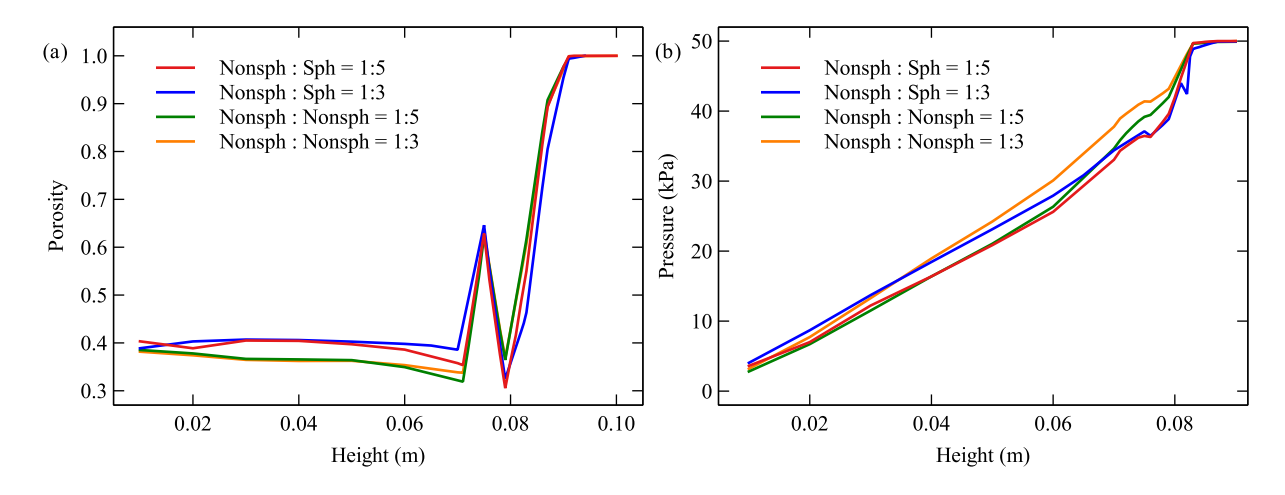


Fig. 27. The evolution of (a) porosity and (b) pressure as functions of height at the final state of the superficial clogging.

 $(\bar{p}=p/p_{max})$  and relative differences  $(|\bar{p}|)$  show consistent 0.1 range regardless of particle shape.

Remarks. The hybrid scheme improves fine particle–fluid interaction management through unresolved components and drag-force models that minimize shape effects. Despite simplification, it captures quantitative and qualitative particle velocity characteristics, including peaks, clogging distribution, and squeezing effects. While showing better qualitative than quantitative pressure accuracy, it captures essential normalized pressure trends. Precision reduction stems from drag-force model differences and grid-cell versus particle-scale interaction lengths

in unresolved schemes, weakening particle-to-fluid velocity constraints and causing pressure discrepancies. For gap-graded particle engineering applications, the hybrid solver offers favorable accuracy–efficiency balance:  ${\sim}33\times$  mesh reduction and  ${\sim}30\times$  performance improvement (3.61 to 0.12 s/timestep).

# 6. Conclusions

We present a hybrid CFD-DEM framework with heterogeneous parallel computing for gap-graded fluid-particle interactions. The framework adaptively integrates unresolved and resolved CFD-DEM solvers

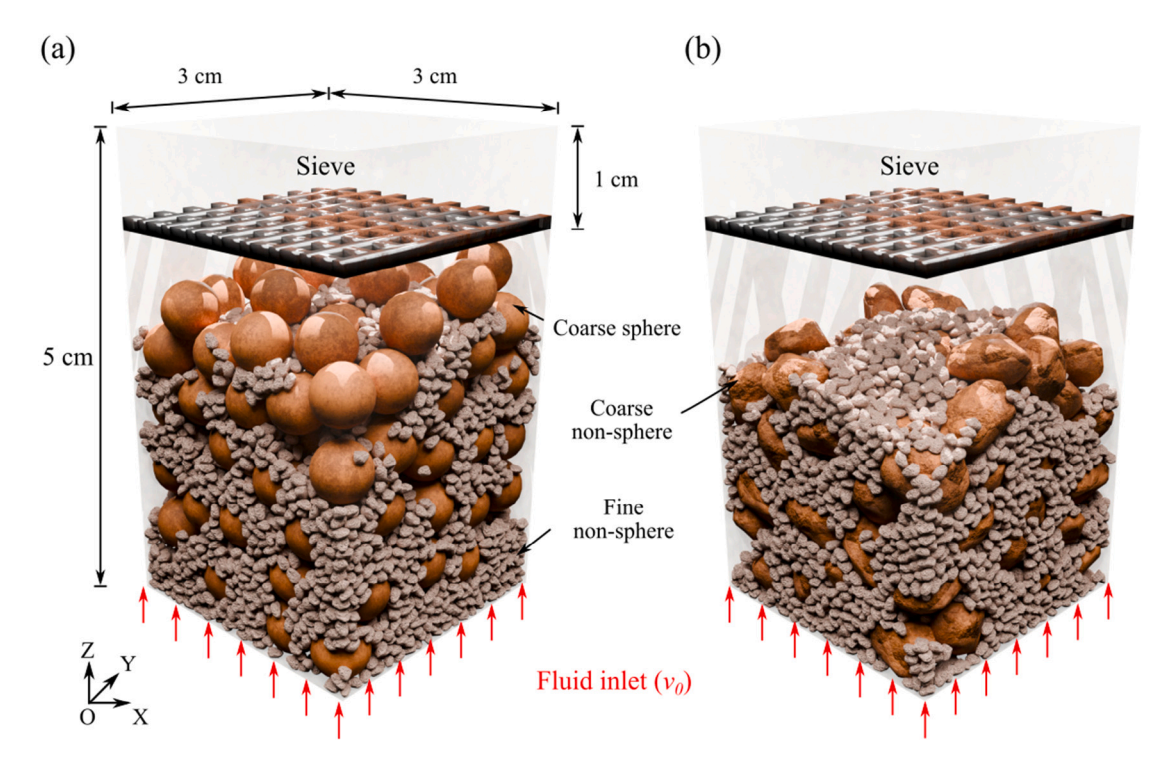


Fig. 28. Simulation preparation for the internal clogging: (a) coarse spheres and fine non-spheres, and (b) coarse non-spheres and fine non-spheres.

across the computational domain based on particle size distributions, effectively balancing computational accuracy and efficiency.

The framework features a Ray-Tracing DEM solver optimized for arbitrary particle shapes in large populations through fine-granularity parallel algorithms. A GPU-accelerated interface tightly couples CFD and DEM solvers, enabling parallel particle geometry encoding from DEM to CFD and efficient hydrodynamic feedback from CFD to DEM. These components enhance scalability and robustness for large-scale complex particle-fluid interaction simulations, supporting dynamic regimes up to the laminar-turbulence transition boundary.

The framework underwent rigorous validation against diverse experimental and analytical benchmarks, testing unresolved, resolved, and hybrid components for spherical and non-spherical particles. Demonstration examples simulated superficial and internal clogging of gapgraded granular materials using all three schemes, enabling comprehensive performance comparison. Results show particle shape significantly influences superficial clogging more than gap size ratio. For internal clogging, the hybrid solver effectively captures fluid squeezing effects from particle clogging (similar to resolved solver) while achieving better balance between computational precision and resource overhead.

# CRediT authorship contribution statement

Hao Chen: Writing - original draft, Visualization, Validation. Shiwei Zhao: Writing - review & editing, Supervision, Funding acquisition. Jidong Zhao: Writing - review & editing, Supervision, Funding acquisition.

## Declaration of competing interest

The authors declare that they have no known competing financial interests or personal relationships that could have appeared to influence the work reported in this paper.

## Acknowledgments

This work was financially supported by National Natural Science Foundation of China (by Project No. 52439001) and Research Grants Council of Hong Kong (by GRF Projects No. 16206322 and No. 16203123, RIF Project No. R6008-24, TRS Projects No. T22-606/23-R and No. T22-607/24N, and YCRF Project No. C6002-24Y). Any opinions, findings, and conclusions or recommendations expressed in this material are those of the authors and do not necessarily reflect the views of the financial bodies.

## Appendix A. The drag force in the unresolved CFD-DEM coupling

The drag force has been well characterized by the Di Felice model [35]. Given a particle i with equivalent diameter  $D_p$ , volume  $V_p$ , and velocity  $U^p$ , submerged in a fluid of density  $\rho_f$ , kinematic viscosity of fluid  $\nu$ , local fluid velocity  $U^f$ , and fluid volume fraction  $\epsilon_f$ , the total drag force  $\mathbf{F}_{i}^{d}$  can be expressed as:

$$F_i^d = \beta_i V_p (U^f - U^p). \tag{A.1}$$

$$\beta_i = \frac{3}{4} \frac{\rho_f |U^f - U^p|}{D_p} C_D \epsilon_f^{(2-\chi)}, \tag{A.2a}$$

$$\begin{split} C_D &= \left(0.63 + \frac{4.8}{\sqrt{Re_p}}\right)^2, \\ \chi &= 3.7 - 0.65 \exp\left(-\frac{1.5 - \log(Re_p)}{2}\right), \end{split} \tag{A.2b}$$

$$\chi = 3.7 - 0.65 \exp\left(-\frac{1.5 - \log(Re_p)}{2}\right),$$
 (A.2c)

$$Re_{p} = \frac{D_{p}|U^{f} - U^{p}|\epsilon_{f}}{v}.$$
(A.2d)

where  $C_D$  represents the drag coefficient, and  $Re_p$  denotes the volumeaveraged particle Reynolds number.

Since unresolved coupling allows a fluid cell to contain multiple particles, the calculation and application of drag force can be categorized into two distinct approaches [91]. The first approach computes

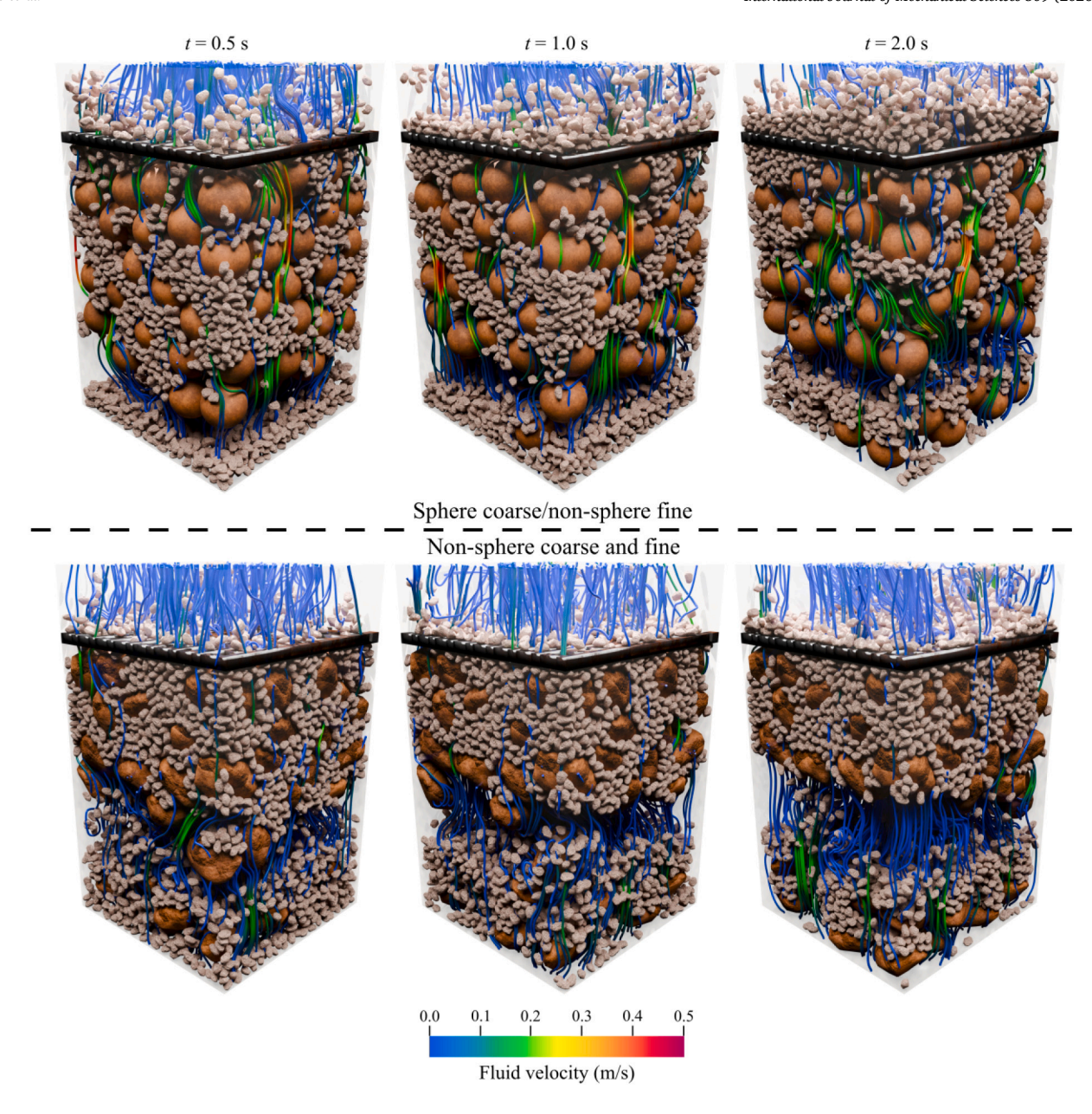


Fig. 29. Simulation snapshots of the coarse sphere/fine non-sphere group (top row) and the coarse non-sphere/fine non-sphere group (bottom row) during the process of internal clogging.

the drag force at the cell level and subsequently distributes it among the individual particles in proportion to their volumetric representation within that cell. In contrast, the second approach calculates the drag force for each particle individually, followed by a weighted distribution to the cells. This study employs the second approach, as Zhou et al. [91] demonstrated that it enhances the robustness of CFD-DEM mechanical interactions, particularly when the ratio of particle size to cell size is variable. For instance, as illustrated in Fig. 2, when two particles, D and E, occupy the same cell, the total drag force on that cell can be expressed as  $F_c = -(f_0 + f_1)$ , since both particles are entirely contained within the cell. However, when a particle, such as particle A, spans multiple cells, a smooth decomposition of the drag force is necessary. This is accomplished using a marker-weighted interpolation scheme, as opposed to the SDF template used in the resolved counterpart. Assuming that particle A's volume is decomposed into four markers, the left-top, left-bottom, and right-bottom cells would receive 0.25,

0.5, and 0.25 of the drag force, respectively. In practical applications, this marker strategy is primarily used for moderate particle-to-cell size ratios, where the number of markers is linearly adjusted according to the ratio.

Once the drag force  $(\sum_i F_i^d)$  calculation on the DEM side is complete, its transfer to the CFD side  $(F_c^d)$  adheres to Newton's third law, expressed in implicit form:

$$F_c^d = \frac{\sum_i F_i^d}{V_c | U_c^f - U_c^p|} (U_c^f - U_c^p).$$
 (A.3)

where  $V_c$  denotes the volume of the fluid cell,  $U_c^p$  represents the cell-averaged particle velocity, and  $U_c^f$  corresponds to the velocity of the fluid cell. By integrating Eq. (A.3) into Eq. (3), the term  $\frac{\sum_i F_i^l}{V_c |U_c^f - U_c^p|} U_c^p$  functions as a source term, while  $\frac{\sum_i F_i^d}{V_c |U_c^f - U_c^p|}$  contributes to the diagonal component of the coefficient matrix.

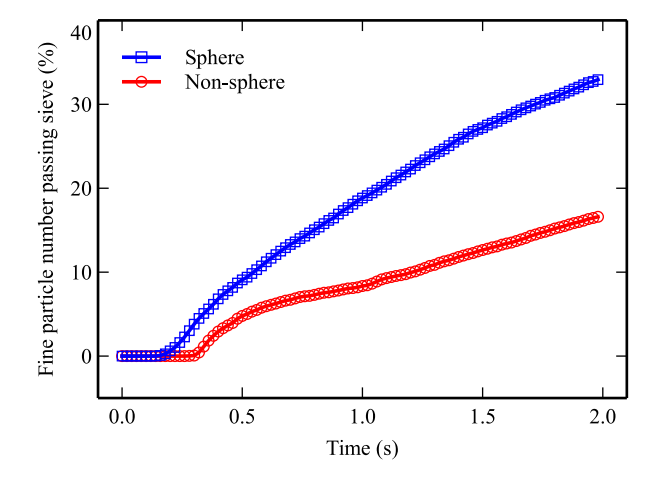


Fig. 30. Percentage of particles number passing through the sieve for spheres group and non-sphere group in the internal clogging simulations.

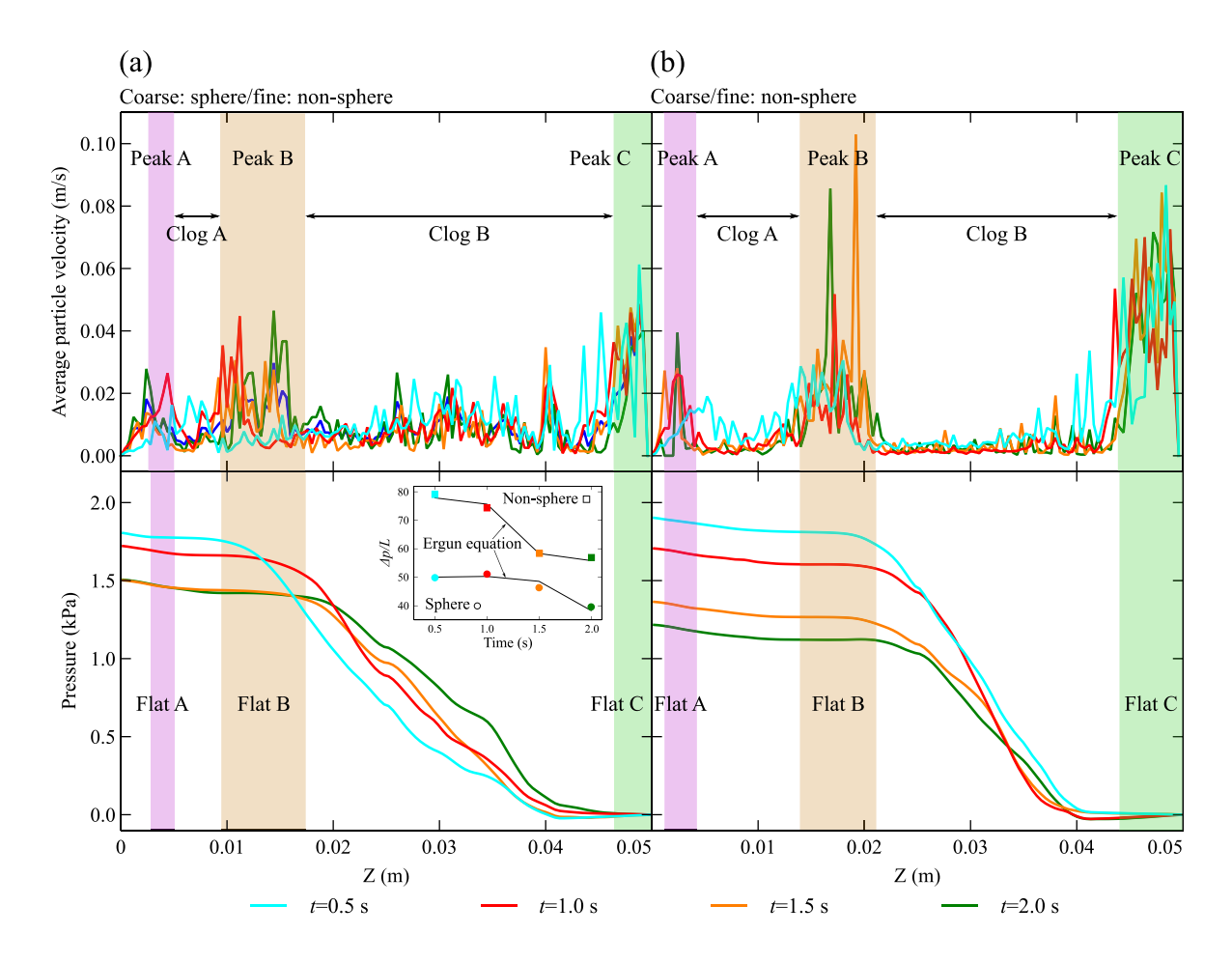


Fig. 31. Evolution of average fine particle velocity (top row) and fluid pressure (bottom row) against the Z-direction for varying time instants in the internal clogging.

# Appendix B. The IB forces in the resolved CFD-DEM coupling

This study introduces a multi-step corrector aimed at improving the precise application of the IB force from CFD to DEM components. This enhancement leverages the widely-used PIMPLE (Pressure IMplicit for Pressure-Linked Equations) scheme in CFD. The IB force scheme initiates with a momentum corrector, which is derived from the Navier–Stokes equation, as presented in Eq. (4b). This equation can be

reformulated as follows:

$$AU_f^* = B, (B.1a)$$

$$\mathbf{A} = \mathbf{A}_D + \mathbf{A}_{ND},\tag{B.1b}$$

$$\mathbf{B} = -\nabla p + \rho \mathbf{g} + \mathbf{F}_{IB}. \tag{B.1c}$$

where A denotes the coefficient matrix derived from the convection term and viscous stress, and its diagonal and non-diagonal components

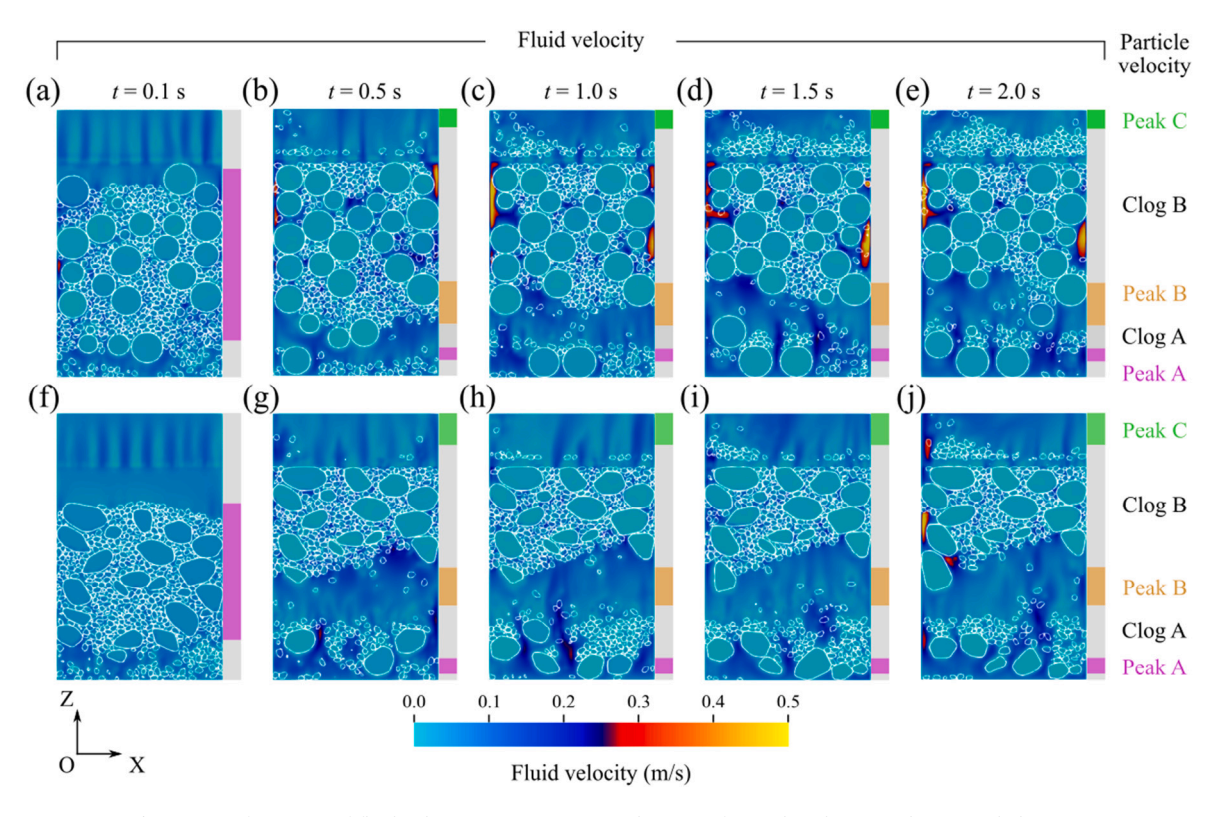


Fig. 32. Configuration of fluid velocity in conjunction with states of particle velocity in the internal clogging.

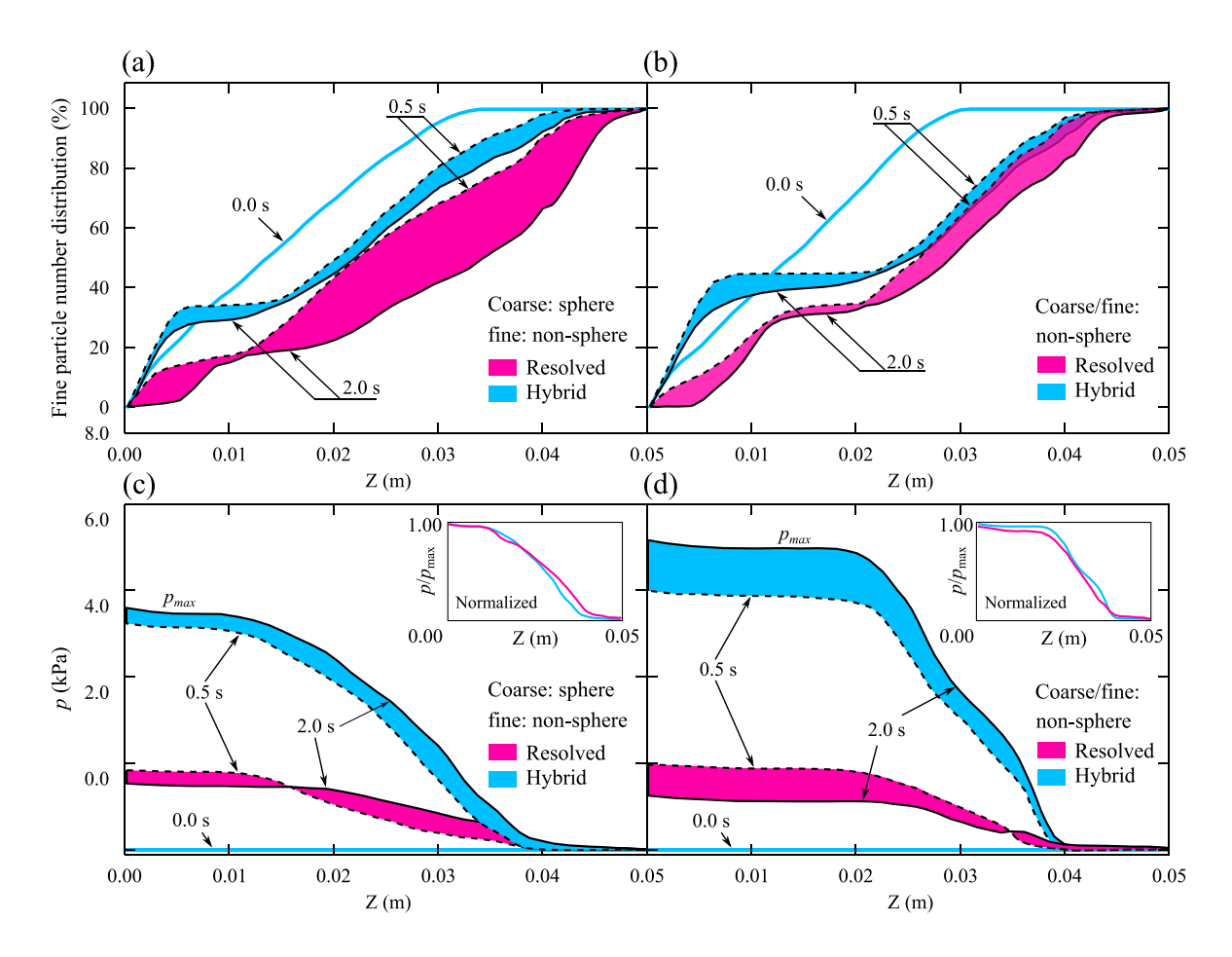


Fig.~33.~Number of particles passing and pressure drop over time: (a,c)~sphere group; (b,d)~non-sphere group in the hybrid internal clogging simulations.

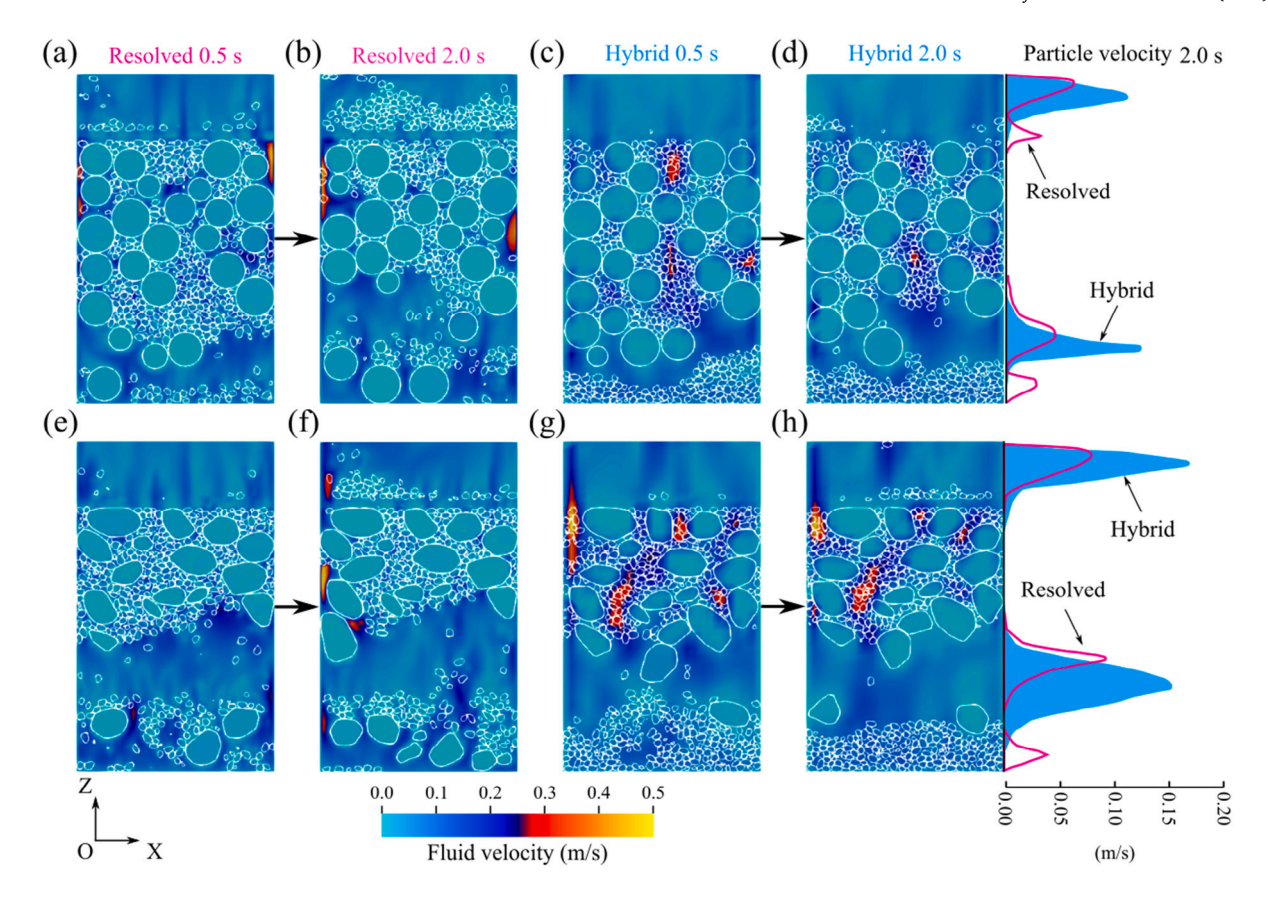


Fig. 34. Snapshots of fluid and particle velocities are presented under both resolved and hybrid coupling schemes for internal clogging: top row illustrates the sphere group, while the bottom row depicts the non-sphere group.

are identified by the subscripts D and ND, respectively;  $U_f^*$  signifies the predicted fluid velocity obtained from the momentum equation; and  $\mathbf{B}$  encapsulates the contributions from the pressure gradient, gravitational force, and immersed force.

Further simplification allows us to modify Eq. (B.1b) by substituting certain unknowns in  $\boldsymbol{U}_f^*$  with the known quantities in  $\boldsymbol{U}_f$ :

$$\mathbf{A}_D \mathbf{U}_f^* + \mathbf{A}_{ND} \mathbf{U}_f = \mathbf{B}, \tag{B.2a}$$

$$\mathbf{A}_D \mathbf{U}_f^* = \mathbf{B} + \mathbf{H},\tag{B.2b}$$

$$U_f^* = \frac{B}{A_D} + \frac{H}{A_D},\tag{B.2c}$$

$$H = -A_{ND}U_f. (B.2d)$$

where  $U_f$  represents the fluid velocity from the previous timestep, while H captures the contributions from the convection term and viscous stress in an explicit manner.

The continuity equation Eq. (4a) refines Eq. (B.2d) into the follow-

$$\nabla \cdot \nabla \frac{p}{\mathbf{A}_{D}} = \nabla \cdot \frac{\mathbf{H} + \rho \mathbf{g}}{\mathbf{A}_{D}} + \nabla \cdot \frac{\mathbf{F}_{IB}^{*}}{\mathbf{A}_{D}},$$

$$U_{f}^{**} = \frac{\mathbf{H} + \rho \mathbf{g}}{\mathbf{A}_{D}} - \frac{\nabla p^{*}}{\mathbf{A}_{D}} + \frac{\mathbf{F}_{IB}^{*}}{\mathbf{A}_{D}}.$$
(B.3a)

$$U_f^{**} = \frac{H + \rho g}{A_D} - \frac{\nabla p^*}{A_D} + \frac{F_{IB}^*}{A_D}.$$
 (B.3b)

where  $\boldsymbol{U}_f^{**}$  denotes the fluid velocity corrected to satisfy the continuity criterion,  $p^*$  represents the predicted pressure, and  $F_{IB}^*$  indicates the updated IB force, which is based on the corrected velocities of both the fluid and the immersed particles.

PIMPLE iterations are designed to incorporate multiple loops, thereby facilitating effective convergence. This procedure starts with the base particle velocity  $U_p$ , which is derived from the previous step, and a

pressure-corrected fluid velocity denoted as  $\boldsymbol{U}_f^{**}$ . From these velocities, a predicted IB force  $F_{IB}^*$  is calculated. Through successive iterations of the IB force correction, the unbalanced dynamics between the solid and fluid progressively converge towards a state of static equilibrium, expressed as follows:

$$F_{IB}^* = F_{IB} + \beta \frac{(U_p - U_f^{**})}{A_D},$$
 (B.4a)

$$F_{IB}^{*} = F_{IB} + \beta \frac{(U_{p} - U_{f}^{**})}{A_{D}},$$

$$U_{p}^{*} = U_{p} - \frac{F_{IB}^{*}}{M_{p}} \Delta t - \vec{r} \times \frac{\vec{r} \times F_{IB}^{*}}{I_{p}} \Delta t.$$
(B.4a)

where  $U_n^*$  represents the corrected particle velocity resulting from the immersed force,  $M_p$  denotes the mass of the particle,  $\vec{r}$  is the position vector from the particle's center of mass to the cell center, and  $I_n$ corresponds to the moment of inertia of the particle. The updated particle velocity further influences a new immersed force through an accumulation and damping behavior, governed by a fractional factor  $\beta$  < 1. In scenarios where the fluid cell loses contact with the particles, the IB force is reset to zero, indicating that no corrections are necessary.

The final iteration of the PIMPLE algorithm provides a conclusive assessment of the IB force, which is used to rectify the interactions between the solid and fluid phases:

$$F_{IB}^{**} = \begin{cases} \frac{(U_p^{**} - U_f^{***})}{A_D}, & \epsilon_f < 1, \\ 0, & \epsilon_f = 1. \end{cases}$$
(B.5)

where  $F_{IB}^{**}$  represents the immersed force, while  $U_p^{**}$  and  $U_f^{***}$  denote the particle velocity and fluid velocity at the final stage of the PIMPLE iteration, respectively. The resultant IB force is designed to ensure adherence to the IB condition for both the preceding and current time steps.

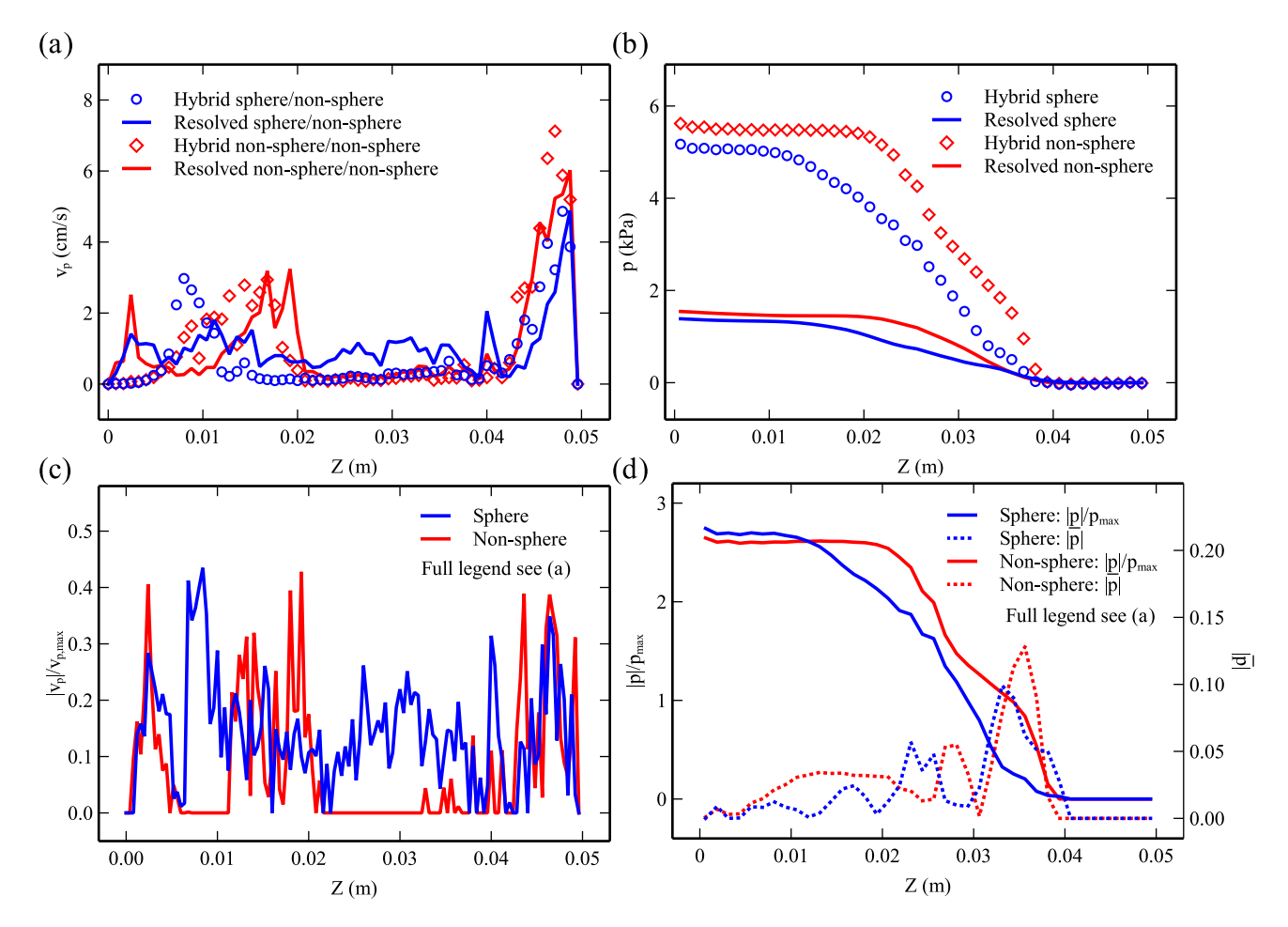


Fig. 35. The averaged values over all time instances for (a) particle velocity, (b) fluid pressure, and the differences between their hybrid and resolved simulation results, specifically for (c) particle velocity and (d) fluid pressure in relation to their maximum values. Note that the difference in normalized fluid pressure is also included in (d).

## Data availability

No data was used for the research described in the article.

# References

- [1] Chen Y, Xiong H, Cheng H, Yu C, Xie J. Effect of particle motion on the hydraulic collection of coarse spherical particles. Acta Mech Sin 2020;36:72–81.
- [2] Liang W, Liang M, Chen R, Qi Z, Zhang Y, Li X, Lin Y. Dynamic responses of undamped oscillator subjected to underwater shock wave. Int J Mech Sci 2025;289:110094.
- [3] Hu X, Wei Y, Wang C. Dynamic characteristics of polar ocean detector passing through the crushed ice zone based on the CFD-DEM method. Int J Mech Sci 2024;271:109304.
- [4] Zhang Z, Yin T, Huang X, Dias D. Slurry filtration process and filter cake formation during shield tunnelling: Insight from coupled CFD-DEM simulations of slurry filtration column test. Tunn Undergr Space Technol 2019;87:64–77.
- [5] Fu Y, Zeng D, Xiong H, Li X, Chen Y. Seepage effect on failure mechanisms of the underwater tunnel face via CFD–DEM coupling. Comput Geotech 2022:146:104591.
- [6] Zeng R, Wang S, Zhang Y, Qu T. CFD-DEM modeling of seepage in foam-conditioned soil. Comput Geotech 2025;177:106818.
- [7] Mu L, Zhang P, Shi Z, Huang M. Coupled CFD–DEM investigation of erosion accompanied by clogging mechanism under different hydraulic gradients. Comput Geotech 2023;153:105058.
- [8] Xiong H, Zhang Z, Yin Z, Chen X, Zhou W. Microscopic origins of shape effects on migration and clogging of fines in porous media using coupled CFD-iDEM. Acta Geotech 2024;19(8):5001–29.
- [9] Doan T, Indraratna B, Nguyen TT, Rujikiatkamjorn C. Coupled CFD-DEM modelling of clogging of granular columns by cohesive fines. Comput Geotech 2025;177:106902.

- [10] Chen F, Jiang S, Xiong H, Yin Z, Chen X. Micro pore analysis of suffusion in filter layer using tri-layer CFD-DEM model. Comput Geotech 2023;156:105303.
- [11] Hu X, Wei Y, Wang C. CFD-DEM analysis of oblique water entry under a polar environment. Int J Mech Sci 2024;278:109480.
- [12] Yu M, Han Y, Jiang L, Qian L, Beaucamp A. Erosion mechanism and surface quality in airflow-driven abrasive microchannel fabrication. Int J Mech Sci 2025;294:110263.
- [13] Moghaddam M, Di Giorgio P, Papini M. Modeling eroded topography in masked abrasive slurry jet pocket milling. Int J Mech Sci 2025;285:109830.
- [14] Ham S-M, Zhang K, Petrie J, Kwon T-H. Coupled CFD-DEM modeling of surface erosion in granular soils: simulation of erosion function apparatus experiments. Can Geotech J 2024;62:1–7.
- [15] Blais B, Lassaigne M, Goniva C, Fradette L, Bertrand F. Development of an unresolved CFD-DEM model for the flow of viscous suspensions and its application to solid-liquid mixing. J Comput Phys 2016;318:201-21.
- [16] Che H, Yue Y, Liu D, Wang S. A voronoi tessellation-based CFD-DEM porosity model for fluidized bed modelling. Adv Powder Technol 2025;36(7):104913.
- [17] Brandt V, Grabowski J, Jurtz N, Kraume M, Kruggel-Emden H. CFD-DEM simulation of a circulating fluidized bed using a particle location based multi-level coarse-graining approach. Powder Technol 2025;121075.
- [18] Hilton J, Cleary P. The influence of particle shape on flow modes in pneumatic conveying. Chem Eng Sci 2011;66(3):231–40.
- [19] Markauskas D, Platzk S, Kruggel-Emden H. Comparative numerical study of pneumatic conveying of flexible elongated particles through a pipe bend by DEM-CFD. Powder Technol 2022;399:117170.
- [20] Van Wachem B, Schouten J, Van den Bleek C, Krishna R, Sinclair J. Comparative analysis of CFD models of dense gas-solid systems. AIChE J 2001;47(5):1035–51.
- [21] Cundall PA, Strack OD. A discrete numerical model for granular assemblies. Géotechnique 1979;29(1):47–65.
- [22] Zhou Z, Zou R, Pinson D, Yu A. Angle of repose and stress distribution of sandpiles formed with ellipsoidal particles. Granul Matter 2014;16:695–709.
- [23] Yao L, Xiao Z, Liu J, Zhang Q, Wang M. An optimized CFD-DEM method for fluid-particle coupling dynamics analysis. Int J Mech Sci 2020;174:105503.

- [24] Liao C-C, Lin M-H, Chung Y-C, Hsu C-C. Dynamic characteristics of granular beds subjected to projectile impact. Int J Mech Sci 2025;110096.
- [25] Zhao J, Zhao S, Luding S. The role of particle shape in computational modelling of granular matter. Nat Rev Phys 2023;5(9):505–25.
- [26] Gallier S, Lemaire E, Lobry L, Peters F. A fictitious domain approach for the simulation of dense suspensions. J Comput Phys 2014;256:367–87.
- [27] Zhao J, Shan T. Coupled CFD-DEM simulation of fluid-particle interaction in geomechanics. Powder Technol 2013;239:248-58.
- [28] Peskin CS. Flow patterns around heart valves: a numerical method. J Comput Phys 1972;10(2):252–71.
- [29] Uhlmann M. An immersed boundary method with direct forcing for the simulation of particulate flows. J Comput Phys 2005;209(2):448-76.
- [30] Yang Y, Wang Y. Enhanced fully resolved CFD-DEM-PBFM simulation of nonspherical particle–fluid interactions during hydraulic collection. Comput Methods Appl Mech Engrg 2024;426:116994.
- [31] Hölzer A, Sommerfeld M. New simple correlation formula for the drag coefficient of non-spherical particles. Powder Technol 2008;184(3):361–5.
- [32] Feng Z, Michaelides EE. A general and accurate correlation for the drag on spherocylinders. Int J Multiph Flow 2023;168:104579.
- [33] Hager A, Kloss C, Pirker S, Goniva C. Parallel resolved open source CFD-DEM: method, validation and application. J Comput Multiph Flows 2014;6(1):13–27.
- [34] Bao Y, Kaye J, Peskin CS. A gaussian-like immersed-boundary kernel with three continuous derivatives and improved translational invariance. J Comput Phys 2016;316:139–44.
- [35] Di Felice R. The voidage function for fluid-particle interaction systems. Int J Multiph Flow 1994;20(1):153–9.
- [36] Zhao F, Van Wachem B. Direct numerical simulation of ellipsoidal particles in turbulent channel flow. Acta Mech 2013;224(10):2331–58.
- [37] Lin X, Ng T-T. A three-dimensional discrete element model using arrays of ellipsoids. Géotechnique 1997;47(2):319–29.
- [38] Chen H, Zhao S, Zhou X. DEM investigation of angle of repose for super-ellipsoidal particles. Particuology 2020;50:53–66.
- [39] Zou R, Yu A-B. Evaluation of the packing characteristics of mono-sized non-spherical particles. Powder Technol 1996;88(1):71–9.
- [40] Zhao S, Zhang N, Zhou X, Zhang L. Particle shape effects on fabric of granular random packing. Powder Technol 2017;310:175–86.
- [41] Wang H, Zhou Y, Zhou B, Zheng W. An investigation of the pressure dip phenomenon within conical sandpiles using CFD-DEM. Powder Technol 2022;398:117152.
- [42] Zhou Z, Pinson D, Zou R, Yu A. Discrete particle simulation of gas fluidization of ellipsoidal particles. Chem Eng Sci 2011;66(23):6128–45.
- [43] Cleary PW, Sawley ML. DEM modelling of industrial granular flows: 3D case studies and the effect of particle shape on hopper discharge. Appl Math Model 2002;26(2):89-111.
- [44] Tenneti S, Garg R, Subramaniam S. Drag law for monodisperse gas-solid systems using particle-resolved direct numerical simulation of flow past fixed assemblies of spheres. Int J Multiph Flow 2011;37(9):1072–92.
- [45] Hilton J, Mason L, Cleary P. Dynamics of gas-solid fluidised beds with non-spherical particle geometry. Chem Eng Sci 2010;65(5):1584–96.
- [46] Shen Z, Wang G, Huang D, Jin F. A resolved CFD-DEM coupling model for modeling two-phase fluids interaction with irregularly shaped particles. J Comput Phys 2022;448:110695.
- [47] Ma S, Wei Z, Chen X. CFD-DEM combined the fictitious domain method with monte carlo method for studying particle sediment in fluid. Part Sci Technol 2018;36(8):920–33.
- [48] Aliu O, Sakidin H, Foroozesh J, Yahya N. Lattice boltzmann application to nanofluids dynamics-a review. J Mol Liq 2020;300:112284.
- [49] Hu G, Zhou B, Shen Z, Wang H, Zheng W. A resolved CFD-DEM investigation on granular sand sedimentation considering realistic particle shapes. Géotechnique
- [50] Wu M, Peters B, Rosemann T, Kruggel-Emden H. A forcing fictitious domain method to simulate fluid-particle interaction of particles with super-quadric shape. Powder Technol 2020;360:264–77.
- [51] Mittal K, Dutta S, Fischer P. Direct numerical simulation of rotating ellipsoidal particles using moving nonconforming schwarz-spectral element method. Comput & Fluids 2020:205:104556
- [52] Lai Z, Zhao J, Zhao S, Huang L. Signed distance field enhanced fully resolved CFD-DEM for simulation of granular flows involving multiphase fluids and irregularly shaped particles. Comput Methods Appl Mech Engrg 2023:414-116195
- [53] Barcet M, Benguigui W, Laviéville J, Benoit M, Wachs A, Fede P, Bonometti T. Resolved DEM-CFD coupling for wave-armour blocks interactions. Ocean Eng 2025;337:121865.
- [54] Zhang X, Tahmasebi P. Investigation of particle shape and ambient fluid on sandpiles using a coupled micro-geomechanical model. Powder Technol 2022;409:117711.
- [55] Wang Y, Yang Y, Yang H, Pang Z. Numerical simulation of fluid-particle interaction in geomechanics using an extended CFD-DEM approach with a superquadric model of non-spherical particles. Int J Numer Anal Methods Geomech 2024;48(1):78–103.

- [56] Wen X, Zheng L, Zhao X, Liu Y, Kang J, Ye G, Wang F, Yuan M, Jiang M. An improved semi-resolved computational fluid dynamics-discrete element method for simulating liquid-solid systems with wide particle size distributions. Phys Fluids 2024;36(3).
- [57] Zhu G, Li H, Wang Z, Zhang T, Liu M. Semi-resolved CFD-DEM modeling of gasparticle two-phase flow in the micro-abrasive air jet machining. Powder Technol 2021;381:585–600.
- [58] Su Z, Xu C, Jia K, Cui C, Du X. A novel semi-resolved CFD-DEM coupling method based on point cloud algorithm for complex fluid-particle systems. Comput Methods Appl Mech Engrg 2025;434:117561.
- [59] Wagner JJ, C. F. Higgs III. Coupled CFD-DEM simulation of interfacial fluid-particle interaction during binder jet 3d printing. Comput Methods Appl Mech Engrg 2024;421:116747.
- [60] Zhao S, Zhao J. Revolutionizing granular matter simulations by high-performance ray tracing discrete element method for arbitrarily-shaped particles. Comput Methods Appl Mech Engrg 2023;416:116370.
- [61] Lai Z, Zhao S, Zhao J, Huang L. Signed distance field framework for unified dem modeling of granular media with arbitrary particle shapes. Comput Mech 2022;70(4):763–83.
- [62] Glowinski R, Pan T-W, Hesla TI, Joseph DD. A distributed lagrange multiplier/fictitious domain method for particulate flows. Int J Multiph Flow 1999;25(5):755–94.
- [63] Wang Z, Teng Y, Liu M. A semi-resolved CFD-DEM approach for particulate flows with kernel based approximation and hilbert curve based searching strategy. J Comput Phys 2019;384:151–69.
- [64] Lorensen WE, Cline HE. Marching cubes: A high resolution 3D surface construction algorithm. SIGGRAPH Comput Graph 1987;21(4):163–9.
- [65] Zhang Y, Ren W, Li P, Zhang X, Lu X. A simple and novel coupling method for CFD-DEM modeling with uniform kernel-based approximation. Comput Part Mech 2024;11(6):2381-97.
- [66] Goniva C, Kloss C, Deen NG, Kuipers JA, Pirker S. Influence of rolling friction on single spout fluidized bed simulation. Particuology 2012;10(5):582–91.
- [67] Weller HG, Tabor G, Jasak H, Fureby C. A tensorial approach to computational continuum mechanics using object-oriented techniques. Comput Phys 1998;12(6):620–31.
- [68] Kloss C, Goniva C, Hager A, Amberger S, Pirker S. Models, algorithms and validation for opensource dem and CFD-DEM, Progress in Computational Fluid Dynamics. Int J 2012;12(2–3):140–52.
- [69] Dalle DJ, Rogers SE, Meeroff J, Burkhead AC, Schauerhamer DG, Diaz JF. Launch vehicle ascent cfd for the space launch system. In: AIAA scitech 2023 forum. 2023, p. 0237.
- [70] Shi Y, Guo N, Yang Z. GeoTaichi: A taichi-powered high-performance numerical simulator for multiscale geophysical problems. Comput Phys Comm 2024;301:109219.
- [71] Gou D, Shen Y. GPU-powered CFD-DEM framework for modelling large-scale gas-solid reacting flows (GPU-rCFD-DEM) and an industry application. Chem Eng Sci 2024;299:120536.
- [72] Stokes G. Liii. remarks on professor challis's paper, entitled "a theory of the composition of colours," & c. The London, Edinburgh, and Dublin. Philos Mag J Sci 1856;12(81):421-5.
- [73] Concha F, Almendra E. Settling velocities of particulate systems, 1. settling velocities of individual spherical particles. Int J Miner Process 1979;5(4):349–67.
- [74] Terzaghi K. Principles of soil mechanics. iv. settlement and consolidation of clay. Eng News-Record 1925;95:874.
- [75] Chen F, Drumm EC, Guiochon G. Coupled discrete element and finite volume solution of two classical soil mechanics problems. Comput Geotech 2011;38(5):638–47.
- [76] Vollmari K, Oschmann T, Kruggel-Emden H. Mixing quality in mono-and bidisperse systems under the influence of particle shape: A numerical and experimental study. Powder Technol 2017;308:101–13.
- [77] Çalışkan U, Mišković S. Analysis of particle dispersion and cavity formation during bulk particle water entry using fully coupled CFD-DEM-VOF approach. Particuology 2024;90:558–80.
- [78] Ten Cate A, Nieuwstad C, Derksen JJ, Van den Akker H. Particle imaging velocimetry experiments and lattice-boltzmann simulations on a single sphere settling under gravity. Phys Fluids 2002;14(11):4012–25.
- [79] Willmarth WW, Hawk NE, Harvey RL. Steady and unsteady motions and wakes of freely falling disks. 1964.
- [80] Fortes AF, Joseph DD, Lundgren TS. Nonlinear mechanics of fluidization of beds of spherical particles. J Fluid Mech 1987;177:467–83.
- [81] Studeník O, Isoz M, Šourek MK, Kočí P. OpenHFDIB-DEM: An extension to openfoam for CFD-DEM simulations with arbitrary particle shapes. SoftwareX 2024:27:101871.
- [82] Grass AJ. Structural features of turbulent flow over smooth and rough boundaries. J Fluid Mech 1971;50(2):233–55.
- [83] Ligrani PM, Moffat RJ. Structure of transitionally rough and fully rough turbulent boundary layers. J Fluid Mech 1986;162:69–98.
- [84] Singh KM, Sandham N, Williams J. Numerical simulation of flow over a rough bed. J Hydraul Eng 2007;133(4):386–98.

- [85] Poletto VG, Barros VSL, De Lai FC, de Almeida Waldmann AT, Martins AL, de Mello Junqueira SL. CFD-DEM modeling and simulation of dynamic filtration over heterogeneous porous medium. Powder Technol 2024;445:120057.
- [86] Ren Y, Mo X, Yang B, Zheng S, Jiang L. Study on textile clogging mechanism based on CFD-DEM method and experiments. Comput Part Mech 2025;1–13.
- [87] Yin T, Zhang Z, Huang X, Shire T, Hanley KJ. On the morphology and pressurefiltration characteristics of filter cake formation: Insight from coupled CFD-DEM simulations. Tunn Undergr Space Technol 2021;111:103856.
- [88] Yu S-W, Bai T-Z, Peng C-H. Clogging analysis of purge flow of a rectangular packed pebble bed in cfetr. IEEE Trans Plasma Sci 2024.
- [89] Ergun S, Orning AA. Fluid flow through randomly packed columns and fluidized beds. Ind Eng Chem 1949;41(6):1179–84.
- [90] Liu Y-J, Yin Z-Y, Huang S, Lai Z, Zhou C. Resolved CFD-DEM modeling of suffusion in gap-graded shaped granular soils. J Geotech Geoenvironmental Eng 2024;150(4):04024008.
- [91] Zhou Z, Kuang S, Chu K, Yu A. Discrete particle simulation of particle-fluid flow: model formulations and their applicability. J Fluid Mech 2010;661:482–510.